High-frequency instabilities of stationary crossflow vortices in a hypersonic boundary layer

Fei Li, Meelan Choudhari, and Pedro Paredes
NASA Langley Research Center, Hampton, Virginia 23681, USA

Lian Duan
Department of Mechanical and Aerospace Engineering,
Missouri University of Science and Technology, Rolla, Missouri 65409, USA
(Received 4 April 2016; published 26 September 2016)

Hypersonic boundary layer flows over a circular cone at moderate incidence angle can support strong crossflow instability in between the windward and leeward rays on the plane of symmetry. Due to more efficient excitation of stationary crossflow vortices by surface roughness, such boundary layer flows may transition to turbulence via rapid amplification of the high-frequency secondary instabilities of finite-amplitude stationary crossflow vortices. The amplification characteristics of these secondary instabilities are investigated for crossflow vortices generated by an azimuthally periodic array of roughness elements over a 7° half-angle circular cone in a Mach 6 free stream. The analysis is based on both quasiparallel stability theory in the form of a partial-differential-equation-based eigenvalue analysis and plane marching parabolized stability equations that account for the effects of the nonparallel basic state on the growth of secondary disturbances. Depending on the local amplitude of the stationary crossflow mode, the most unstable high-frequency disturbances either originate from the second (i.e., Mack) mode instabilities of the unperturbed boundary layer or correspond to genuine secondary instabilities that reduce to stable disturbances at sufficiently small amplitudes of the stationary crossflow vortex. The predicted frequencies of the dominant secondary disturbances of either type are similar to those measured during wind tunnel experiments at Purdue University and the Technical University of Braunschweig, Germany. Including transverse surface curvature within the quasiparallel predictions does not alter the topology of the unstable modes; however, the resulting changes in both mode shape and disturbance growth rate are rather significant and curvature can be either stabilizing or destabilizing depending on the disturbance frequency and mode type. Nonparallel effects are shown to be strongly destabilizing for secondary instabilities originating from both Mack modes and instabilities of the inclined shear layer bounding the crossflow vortex. Consequently, the two types of instabilities are found to achieve logarithmic amplification factors of up to $N = 10$ and $N = 7$, respectively. Results also reveal possible phase synchronization between a pair of modes that may have a significant influence on their overall amplification.

DOI: 10.1103/PhysRevFluids.1.053603

I. INTRODUCTION

By virtue of its influence on surface heat transfer, skin friction, and separation characteristics, the boundary layer transition from a laminar to a turbulent state can have a major impact on the design and performance of hypersonic flight vehicles. The transition over realistic vehicle surfaces is often caused by surface roughness of sufficiently large amplitude. However, when the surface is relatively smooth, the laminar-turbulent transition process is initiated by linear instabilities of the laminar boundary layer. Typically, the second (or Mack) mode instability dominates transition in two-dimensional (2D) or axisymmetric boundary layers at hypersonic speeds [1], although centrifugal (i.e., Görtler) instabilities may also come into play when the body surface has concave curvature along the streamwise direction [2]. Three-dimensional boundary layers involve the additional mechanisms

of stationary and traveling modes of crossflow instability [3] and, depending on the geometric configuration, the attachment line instability as well.

Regardless of the speed regime, linear stability correlations have been quite successful in predicting the onset of transition when a single instability mechanism dominates the transition process. Mixed mode transition has been more difficult to predict. Furthermore, measurements of crossflow instability in low-speed boundary layers have exposed the shortcomings of applying purely linear predictive models to transition in 3D boundary layers by revealing the importance of nonlinear effects during crossflow dominated transition [3]. The canonical configuration of a circular cone at the angle of attack includes the necessary elements to study both the mixed mode transition and crossflow development in the context of both supersonic [4–12] and hypersonic [13–31] boundary layer flows. Instability mechanisms for the boundary layer flow over an elliptic cone have been investigated in Refs. [19,29,32–45]. While the elliptic cone configuration supports instability mechanisms similar to the circular cone at an angle of incidence, the details of transition patterns can be different as noted in Ref. [40].

The availability of low-disturbance (i.e., quiet) hypersonic facilities opens up the possibility of a detailed study of the above-mentioned instability phenomena in a controlled environment [21–25]. However, because of the complexity of the crossflow transition process, the interpretation of wind tunnel measurements must be guided by synergistic computations of the flow field and its stability characteristics. The objective of this ongoing effort is to help provide the required characterization in support of wind tunnel experiments so as to eventually resolve some of the outstanding issues related to transition mechanisms in three-dimensional hypersonic boundary layers over nominally smooth surfaces. The present paper represents an initial step in that direction as described below.

The development of stationary and traveling crossflow instabilities on circular and elliptic cone configurations at a free-stream Mach number of 6.0 has been addressed in Refs. [17–30]. Limited measurements of traveling crossflow instability by Borg *et al.* [46] have yielded an encouraging comparison with the linear stability predictions by Li *et al.* [19]. More recent quiet tunnel experiments indicate that similar comparisons may soon be possible for the stationary crossflow modes as well. In particular, experimental measurements of crossflow instability over a yawed circular cone in two different Mach 6 quiet wind tunnels have been reported recently. Each of these investigations is rather remarkable, albeit for different reasons. Ward *et al.* [21] performed measurements using temperature-sensitive paint (to measure time-averaged surface heat transfer) and dynamic surface pressure transducers at a variety of flow conditions ($\alpha = 3^\circ$ and 4°, $\mathrm{Re} = 9.84 \times 10^6$ to 12.01×10^6, both with and without surface roughness, and a range of axial and azimuthal locations of unsteady pressure sensors) to provide strong evidence of secondary instability. Craig and Saric [25] performed in-depth hot wire measurements of the boundary layer flow over a selected range of azimuthal locations at a fixed free-stream condition. The unsteady pressure spectra measured by Ward *et al.* [21] in the BAMQT facility at Purdue University showed two major peaks at most of the measurement locations and flow conditions with $\alpha = 3^\circ$ and 4°. The lower-frequency peak near 40–50 kHz was attributed to traveling crossflow modes and the higher-frequency peak ranging from 125 to 500 kHz (i.e., nearly three to ten times the frequency of the lower peak) was attributed to the secondary instability of stationary crossflow modes. A limited set of wind tunnel runs showed an additional, intermediate-frequency peak near 150 kHz, but the character and the origin of the fluctuations associated with this peak could not be established. Subsequent measurements by McKiernan *et al.* [22] and Edelman and Schneider [23] extended the above measurements to $\alpha = 6^\circ$. For a narrower set of sensor locations, the peak frequency of the measured surface pressure spectra was between 300 and 335 kHz. The peak frequency decreased slightly as the sensor location shifted downstream.

The hot wire measurements by Craig and Saric [24,25] in the NASA Langley Mach 6 quiet tunnel at Texas A&M University provided quantitative maps of steady and unsteady mass-flux distributions across the cross section of the stationary crossflow vortices at selected axial locations within the range of $X = 0.35$–0.4 m and azimuthal locations of ϕ between 112° and 124° relative to the windward plane of symmetry. Similar to the Purdue measurements [21–23], they observed two peaks in the frequency spectra. The low-frequency peak over 15–60 kHz was approximately consistent with the

surface pressure spectra of Ward *et al.* [21]. However, the high-frequency peak in the unsteady hot wire measurements involved significantly lower frequencies of 80–130 kHz. The high-frequency disturbances were concentrated over the inclined shear layer that is visible from the overturning stationary mass-flux contours produced by the finite-amplitude stationary crossflow vortices. The measured mode shapes were remarkably similar to the secondary instability mode driven by the azimuthal shear induced by the stationary vortex. According to Craig and Saric [25], the frequency of the azimuthal-shear mode of secondary instability scales like $2U_e/\delta$ in low-speed flows, which is equal to 120 kHz for the conditions of their measurement. Thus, the frequency range of measured high-frequency disturbances in their experiment was in line with this estimate. Computations by Oliviero *et al.* [26] indicated qualitative similarities to the stationary crossflow modes measured in Ref. [25]; however, significant quantitative differences were apparent in the disturbance amplitudes as well as mass-flux contours.

Conventional facility measurements analogous to the quiet-tunnel measurements at Purdue University have been reported by Munoz *et al.* [20]. They used infrared measurements of surface temperature to infer heat transfer and surface pressure measurements to infer the frequencies, amplitudes, and wave angles of instability wave packets over a Mach 6 yawed circular cone tested at the Technical University of Braunschweig. The average spatial extensions of these packets were also mapped out using circumferential cross correlations. For sensors near $\phi = 90^\circ$ from the windward ray and X locations between 0.21 and 0.36 m, the low-frequency lobe was spread over the range between 20 and 50 kHz and the high-frequency peak was centered at approximately 300–350 kHz. These frequency values are remarkably similar to those measured under quiet conditions and therefore, even though Munoz *et al.* attributed the high-frequency peak to possible second-mode instability, it is possible that this peak was actually associated with secondary instabilities of the distorted mean flow in the presence of strong stationary crossflow vortices. At the larger azimuthal angle of 110°, Munoz *et al.* noted higher disturbance amplitudes and slightly reduced center frequency of the high-frequency lobe, analogous to the measurements of Ward *et al.* [21]. Nonlinear interactions between the low-frequency disturbances (traveling crossflow modes) and the high-frequency disturbances (attributed to second-mode perturbations) were also inferred at the most downstream measurement location ($X = 0.36$ m) by using bicoherence analysis. Analysis of cross correlations between multiple pressure transducers indicated that the dominant propagation angle associated with the low-frequency disturbances was between 60° and 70° relative to the flow velocity at the edge of the boundary layer.

Computations of secondary instability of crossflow modes in a hypersonic boundary layer were first reported by Li *et al.* [29]. The predicted secondary instabilities with the highest growth rates had frequencies that were comparable to those measured in the Purdue experiments [21–23], but the computations also revealed the existence of less unstable modes with lower disturbance frequencies that were comparable to those measured by Craig and Saric [25]. The unstable secondary modes were shown to have an intricate variety of modal structures, with fluctuations concentrated in various subregions of high shear associated with the stationary crossflow structures. In general, no dominant modes with spatial concentration on the top of the inclined shear layer (the mode shape typically associated with the wall-normal shear of the basic state) were found. However, the analysis of Li *et al.* [29] was limited to local secondary instability analyses at selected stations and hence did not provide any information about the integrated amplification of the secondary disturbances. Recently, more detailed secondary instability analyses of large-amplitude stationary crossflow vortices developing between the windward and leeward lines were carried out by Li *et al.* [30] and Moyes *et al.* [31]. These works revealed the complex nature of the secondary instability characteristics by identifying three major types of instability modes: traveling crossflow and Mack mode instabilities present in the unperturbated boundary layer, but modulated by the presence of large-amplitude stationary crossflow vortices, and genuine secondary instability modes that arise because of the presence of large-amplitude stationary crossflow vortices. The major difference, in terms of methodologies employed, between the two analyses was that, in the former computations, the base flow of stationary crossflow vortices was computed via direct numerical

simulation (DNS), while in the latter, the base flow was computed by nonlinear parabolized stability equations.

The present paper describes the analysis of high-frequency instability modes supported by stationary crossflow vortices over a Mach 6 circular cone, including a limited account of the effects of transverse curvature of the cone surface and nonparallelism of the basic state. The emphasis of the paper is on identifying and characterizing the various modes supported by the relatively complex crossflow pattern superposed over an azimuthally inhomogeneous, i.e., fully three-dimensional, basic state. To enhance the utility of this analysis, the computational parameters are chosen to enable both qualitative comparisons with previous wind tunnel experiments (with uncontrolled forcing) and quantitative comparisons with potential future experiments (with controlled forcing). Because of the uncontrolled excitation of crossflow vortices in recent experiments [20,21,23,25], the computations do not seek a perfect match with either of them. Instead, the DNS aims to mimic the approximate wavelength and amplitude range of the measured crossflow vortices by using a relatively simple controlled forcing at an upstream axial direction so that the results can provide further insights into the available measurements of high-frequency fluctuations. Furthermore, the controlled forcing used in the DNS can be easily implemented on a wind tunnel model and we hope that the present analysis will prompt future experiments that can provide an *a posteriori* validation of the computational results.

The remaining sections of this document are laid out as follows. A brief summary of the flow configuration of interest is given in Sec. II, which also describes the analysis codes used in this study. Nonlinear evolution of stationary crossflow modes using direct numerical simulations is described in Sec. III A and the high-frequency secondary instability of these finite-amplitude crossflow vortices is investigated in Sec. III B. A summary is presented in Sec. IV.

II. FLOW CONFIGURATION AND ANALYSIS CODES

The flow configuration of interest corresponds to a circular cone at angle of attack to a uniform, hypersonic free stream. The primary configuration for the Purdue experiments corresponds to a 0.457-m-long (18 in.), nominally-sharp-nosed cone (modeled with a nose radius of 10^{-4} times the cone length) with a half angle of 7° and an angle of attack α equal to 6°. The free-stream conditions correspond to a free-stream Mach number of $M = 6$, unit Reynolds number $\mathrm{Re} = 10.8 \times 10^6$ per meter, and free-stream temperature $T_\infty = 52.44\,\mathrm{K}$. The temperature of the model surface T_w is equal to 300 K.

The unperturbed boundary layer flow over the cone is computed using the viscous upwind algorithm for complex flow analysis (VULCAN) software [47]. The code solves the unsteady conservation equations appropriate for laminar or turbulent flow of calorically or thermally perfect gases with a spatially-second-order accurate cell-centered finite-volume scheme. A variety of upwind schemes are available for fine-tuning of numerical dissipation and shock capturing in order to ensure solution accuracy for stability computations. In the present computations, the inviscid fluxes were constructed using the monotonic upstream-centered scheme for conservation laws $\kappa = 0$, the van Albada gradient limiter [48], and the low-dissipation flux split scheme of Edwards [49]. The cell face gradients required to construct the viscous fluxes were obtained using an auxiliary control volume approach that results in a compact viscous stencil that produces a second-order accurate approximation of the full Navier-Stokes viscous fluxes. The solutions were relaxed in pseudotime to steady state using the 3D ILU(0) scheme [50] with a constant Courant-Friedrichs-Lewy number on the order of 50. Grids of $545 \times 257 \times 353$ and $273 \times 129 \times 353$ in the axial, azimuthal, and wall-normal (or radial) directions, respectively, were used. Exploiting the azimuthal symmetry of the boundary layer about the windward and leeward planes, only one half of the circular cone was modeled in the boundary layer computation. In previous work, similar computations of the mean flow over an elliptic cone configuration were cross-validated against the solutions obtained with the LAURA code [51] for various grid sizes [20]. Thus, no extensive grid convergence analysis was deemed necessary. As an illustration, however, Fig. 1 shows the boundary layer profiles obtained using two different grids. The profiles of the axial velocity component u are plotted for selected

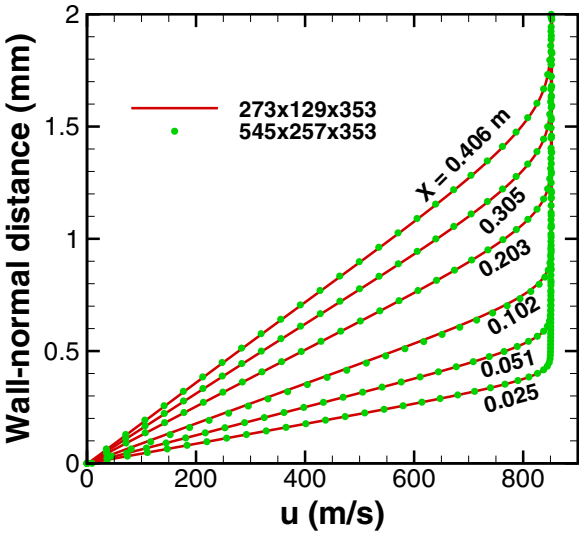

FIG. 1. Effect of grid resolution on mean velocity profiles along $\phi = 120^\circ$.

axial locations (indicated by the value of X for each curve) along the $\phi = 120^\circ$ ray, where ϕ denotes the azimuthal angle measured from windward to leeward ray. Excellent agreement may be observed between the two sets of profiles across the entire length of the cone. Further details on the mean flow solution and its linear stability characteristics may be found in Ref. [17].

The evolution of stationary crossflow disturbances in the boundary layer flow is computed by solving the fully-three-dimensional compressible Navier-Stokes equations in conservation form. The VULCAN solution described above is injected as the basic state for the computation of nonlinear crossflow vortices. The differences in numerical schemes used for the basic state and crossflow vortex computations are accommodated via a stationary body force that corresponds to the residual of the VULCAN solution injected into the DNS code. To provide a controlled setting for the study of secondary instability, the stationary crossflow vortices are excited via azimuthally periodic forcing with a single azimuthal wave number of $n = 60$, where n denotes the number of vortex wavelengths across the full circumference of the circular cone. The forcing is introduced via an array of localized roughness elements centered at $X = 0.18$ m. The streamwise shape of the roughness elements corresponds to a half-wavelength cosine shape with an axial wavelength of 0.008 m and a peak height perturbation of 5 μm.

Due to a lack of controlled excitation of crossflow vortices in the experiments, the measured vortex patterns in Refs. [20,21,23,25] represent the outcome of forcing from an unknown disturbance environment that is presumably dominated by contributions from the surface roughness. Thus, matching the exact details of vortex patterns in the experiments is neither possible nor desired during the present study and the DNS merely seeks to produce a vortex pattern with comparable spacing and strongly nonlinear vortex amplitudes that are analogous to the available measurements near the end of the cone, namely, velocity contours resembling the measurements of Craig and Saric [25] and heat flux variations that are comparable to the measurements of Edelmann and Schneider [23]. The primary focus of the present study is to characterize the general behavior of secondary instabilities of stationary crossflow vortices in a hypersonic boundary layer, and for that purpose, it is sufficient that the crossflow vortices approximate the observed spacing and the strength of nonlinear crossflow vortices as gauged by the rollup of mass-flux contours across the cross section and the spatial region (axial and azimuthal locations) of vortices with sufficiently large amplitudes. In other words, the role of the roughness-induced forcing in this paper is simply to mimic the overall effects of the complex receptivity process on the experimental model via a relatively simple forcing. To that end, we choose

to excite an initially periodic pattern of vortices that undergoes a large enough amplification due to crossflow instability to exhibit the targeted characteristics of crossflow vortices on the experimental models. Alternately, we note that the chosen forcing is also easy to implement in future experiments, provided the model surface has been polished sufficiently so as to minimize the extra forcing from the natural surface roughness.

The working fluid is assumed to be perfect gas (air) and the usual constitutive relations for a Newtonian fluid are used: The viscous stress tensor is linearly related to the rate-of-strain tensor and the heat flux vector is linearly related to the temperature gradient through Fourier's law. The coefficient of viscosity is computed from Sutherlands's law and the coefficient of thermal conductivity is computed by assuming a constant Prandtl number $\mathrm{Pr} = 0.71$. A detailed description of the governing equations and their numerical solution is given by Wu and Martin [52]. The inviscid fluxes from the governing equations are computed using a seventh-order weighted essentially nonoscillatory (WENO) finite difference introduced by Jiang and Shu [53] and the present scheme is optimized by means of limiters [52,54] to reduce the numerical dissipation. Both an absolute limiter on the WENO smoothness measurement and a relative limiter on the total variation are employed simultaneously during the simulation. The viscous fluxes are discretized using a fourth-order central-difference scheme and time integration is performed using a third-order low-storage Runge-Kutta scheme [55]. The numerical code has been previously applied to simulation of turbulence in hypersonic boundary layers [56] as well as laminar-turbulent transition due to crossflow instability in swept wing boundary layers [57,58]. The lessons learned from these simulations were applied to develop the computational grid for stationary crossflow evolution in the present work.

The primary instability computation is performed on a grid consisting of $600 \times 1200 \times 140$ points in the axial (X), azimuthal (ϕ), and wall-normal (Y) directions, respectively. Without any loss of generality, the stationary crossflow disturbances are assumed to be symmetric about the windward and leeward planes, so only one half of the circular cone was included in the computational domain. The grid points are spaced uniformly in the azimuthal direction. The numerical accuracy of the basic state calculation was verified *a posteriori* by using a $600 \times 1800 \times 200$ grid with significantly higher resolution in the azimuthal and radial directions. The axial resolution was kept the same because a visual inspection of the computed solution indicated that the relatively slow axial evolution was adequately captured by the baseline grid. Excellent agreement between the two solutions was found even in the relatively stringent comparisons involving velocity contours across the cross-sectional area of the crossflow vortices. Additional comparisons between the solutions obtained from these two grids will be presented in Sec. III below.

The secondary instability of the finite-amplitude stationary crossflow vortices computed using DNS is investigated using two different methods. The first method corresponds to a quasiparallel analysis of spatial instability as described by Li and Choudhari [59,60], whereas the second technique accounts for the leading-order nonparallel effects using the framework of parabolized stability equations (PSEs) as described by Paredes and co-workers [61,62].

A majority of the results presented in this paper are based on the quasiparallel, local eigenvalue analysis. Unlike the earlier results by Li *et al.* [30], which used a mixture of temporal and spatial eigenvalue analysis (used to describe modal topologies and amplification ratios, respectively, of the unstable disturbances), the results in this paper are based purely on the spatial theory, which is now accepted as the more realistic representation of convective disturbance evolution in practice. Because the wavelength of the crossflow instability is comparable to the thickness of the boundary layer, the neglect of transverse curvature is consistent with the high-Reynolds-number asymptotic limit underlying the boundary layer approximation. Instability analysis in the absence of surface curvature amounts to unrolling the cone surface onto a plane. If one were to coat the cone with paint and roll it on a flat surface, the resulting printed area in the shape of a fan would represent the cone-to-plane mapping [Fig. 2(a)], with a one-to-one correspondence between the points on the cone and those on the unrolled flat surface. The left half of Fig. 2(b) shows the axial velocity contours in a subset of a typical cross section of the cone in the presence of stationary crossflow vortices and its map

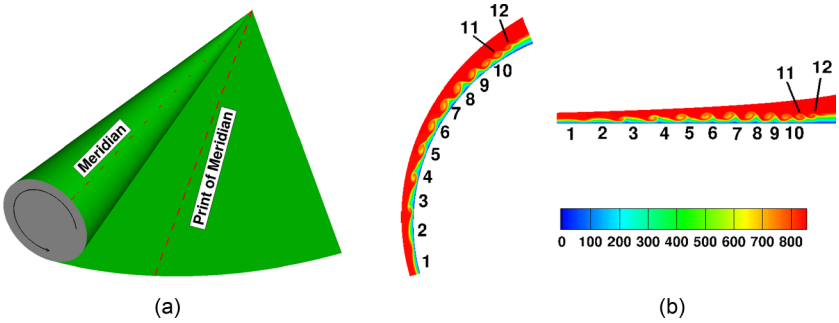

FIG. 2. Schematic of quasiparallel secondary instability analysis. (a) Surface unrolling on a plane. The two dashed lines represent a meridian line on the cone and its imaginary print on the plane, respectively. (b) Correspondence between original and unrolled domains at a given X along with streamwise velocity contours. Vortex 1 is closest to the windward plane ($\phi = 0^\circ$), whereas vortex 12 is closest to the leeward plane ($\phi = 180^\circ$).

onto a domain resting on the flat unrolled surface is shown in the right half of Fig. 2(b). For later reference, the vortices most easily discernible from their surface signature are numbered 1–12 in the figure. The azimuthal extent of each vortex at a given axial station is determined by the distance between the two points on either side of the vortex where the wall shear in the meridian direction is a local maximum. The vortex is then made spanwise periodic via detrending and Fourier low-pass filtering to facilitate local secondary instability computations. In the computational volume with the flattened (i.e., unrolled) base, the X direction is taken as the meridian direction, i.e., the direction along any line joining a point on the flat surface and the virtual vertex of the fan. The local spanwise direction at a point is along the azimuthal coordinate at a fixed axial location over the surface of the cone. The mean flow resulting from these modifications is now amenable to both temporal and spatial stability analyses using the procedure described in Refs. [59,60] in the context of crossflow modes in swept wing boundary layers.

Because the mean flow modified by the presence of crossflow vortices involves comparable length scales in both the azimuthal and radial directions [see Fig. 2(b)], the basic state for secondary instability is inhomogeneous in two spatial directions. Hence, predicting the amplification characteristics of secondary instability modes leads to a planar (i.e., 2D), partial-differential-equation-based eigenvalue problem after invoking the quasiparallel approximation for the basic state [59,60], rather than an ordinary-differential-equation-based eigenvalue problem that is obtained in a classical analysis of primary instabilities in a shear flow that has strong gradients only along the wall-normal coordinate. To incorporate nonparallel flow effects, a suitable generalization of the above procedure to plane marching PSEs as described by De Tullio *et al.* [62] was used. Both quasiparallel and PSE formulations for secondary instability can be extended to include the effects of transverse curvature of the cone surface and calculations were performed to assess the effect of curvature terms with and without the nonparallel mean flow. Quasiparallel formations with no curvature and with curvature terms are denoted by QPNC and QPWC, respectively. The selection of the grid and other aspects of the numerical calculations involving secondary instability analyses were based on extensive experience with a similar class of flows (see, for instance, Refs. [63,64]). Checks were made by using multiple wall-normal and azimuthal grids, wall-normal discretization of orders 4 and 6, and azimuthal discretization based on both sixth-order finite-difference and Fourier differentiation matrices so as to ensure that the impact of variations with respect to those choices was negligible. Typically, the 2D eigenvalue problem corresponding to linear secondary instability was solved by using 121–201 points along the wall-normal direction and between 33 and 65 grid points along the azimuthal direction depending on mode type and stationary vortex amplitude. Selected results demonstrating the lack of grid sensitivity in both basic state calculations and secondary instability characteristics are included in Sec. III below.

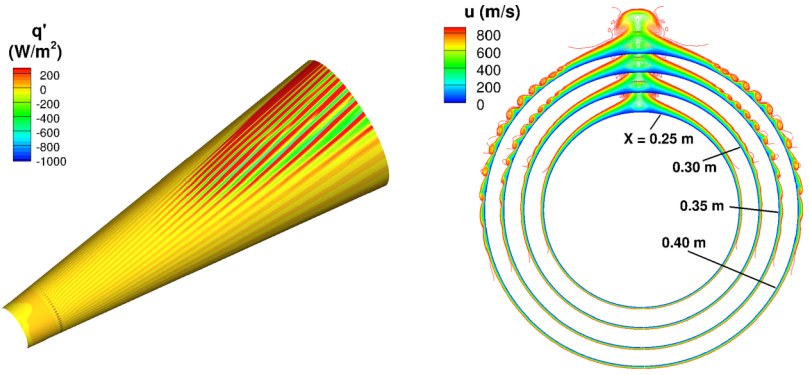

FIG. 3. Evolution of stationary crossflow vortices excited by an azimuthally periodic array of localized roughness elements: (a) contours of wall heat flux perturbation and (b) axial velocity contours at selected locations.

The present paper is a theoretical modeling of high-frequency secondary instabilities of crossflow vortices in a hypersonic boundary layer. To that end, the quasiparallel, no-curvature predictions, which extend the previous state of the art from similar analyses of primary instabilities in a fully 3D boundary layer (based on an ordinary-differential-equation-based eigenvalue problem) to secondary instabilities (using a partial-differential-equation-based eigenvalue analysis), and the studies of secondary instability of crossflow vortices from spanwise periodic patterns in subsonic and supersonic flows to quasiperiodic patterns in hypersonic boundary layers form the appropriate framework for the presentation of these results. The quasiparallel results also provide the crucial foundation for a limited assessment of the effects of surface curvature and mean-flow nonparallelism.

III. RESULTS

Computational results pertaining to both primary and secondary instabilities of the boundary layer flow over the cone are presented in this section. The evolution of stationary crossflow vortices excited by an azimuthally periodic array of localized roughness elements is described first in Sec. III A. The instability characteristics of selected vortices are investigated in Sec. III B.

A. Evolution of stationary crossflow vortices

The stationary crossflow vortices leave an imprint on the cone surface in the form of longitudinal streaks in the surface heat transfer as shown in Fig. 3(a). Immediately downstream of the forcing location, the vortex wavelength is approximately uniform along the azimuthal direction and corresponds to the forcing wave number of $n = 60$. The latter wave number was chosen to approximate the azimuthal wavelength of the crossflow modes found in the experiments of Craig and Saric [25]. Farther downstream from the forcing location, the streaks generated by the roughness element pattern progressively move towards the leeward ray and the streak spacing changes as a result of nonparallel flow effects. Consequently, there is a pronounced difference between the larger vortex wavelength near the sideline ray and the smaller wavelength on the leeward side.

Axial velocity contours at selected streamwise stations are shown in Fig. 3(b). For the forcing location selected in this study ($X = 0.18$ m), the dominant crossflow vortices near the end of the computational domain lie between the sideline ray ($\phi = 90^\circ$) and the leeward ray ($\phi = 180^\circ$), analogous to that in the previously mentioned experimental investigations [21–25]. We note that the prominent vorticity structure centered on the leeward ray is the result of upwelling induced by the secondary flow converging upon the leeward plane from both sides. It is part of the basic state

associated with cones at the angle of attack and does not represent a crossflow instability. The velocity contours at $X = 0.35$ and 0.40 m reveal the strongly nonlinear structure of crossflow vortices that qualitatively resembles the hot wire measurements of Craig and Saric [25]. Figure 3(b) shows a clear trend of decreasing vortex spacing at larger azimuthal angles, i.e., closer to the leeward plane of symmetry. This trend has an effect on the relative importance of azimuthal and radial gradients of the basic state, hence it is also expected to influence the secondary instability characteristics of the stationary crossflow vortices.

Trajectories of selected vortices and the corresponding evolution of vortex amplitudes along the length of the cone are shown in Figs. 4(a)–4(c), respectively. Vortices 6–10 correspond to the highest-velocity perturbations among those shown in Fig. 4(a). The amplitude plotted in Fig. 4(b) corresponds to the peak axial velocity perturbation over the cross section of the vortex, whereas the vortex amplitude shown in Fig. 4(c) corresponds to the peak heat flux perturbation. Results based on a denser grid in the radial and azimuthal directions (1800 and 200 points, respectively, in comparison to 1200 and 140 points in the baseline grid) are also shown to demonstrate the lack of grid sensitivity in the computed stationary crossflow vortices.

Over most of the region shown in Fig. 4(b), vortex 6 has the highest-velocity perturbation of all vortices. However, the vortex 6 amplitude decreases rapidly beyond the location of its peak, whereas the amplitudes of vortex 8 and vortex 10 decrease somewhat after reaching their respective peaks and then the amplitude of vortex 8 starts to increase again. As a result, vortex 8 becomes stronger than vortex 6 at the very end of the computational domain. At $X = 0.25$ m, all three vortices have relatively small amplitudes, less than approximately 2% of the freestream velocity. By $X = 0.30$ m, the vortex amplitudes have increased to somewhere between 5% and 8%, whereas by $X = 0.35$ m, all three vortices have amplitudes in excess of 25%. The peak amplitude achieved by vortex 8 near $X = 0.35$ m is almost 45% of the freestream velocity. The streamwise evolution of the heat flux amplitudes in Fig. 4(c) is similar to that of the corresponding velocity amplitudes in Fig. 4(b). More important, the peak values of the heat flux amplitudes are comparable to those measured in the experiments at Purdue University [21,23,65]. Figure 4(d) displays the effect of enforcing periodicity on the basic state velocity contours for vortex 10 at two different axial locations $X = 0.33$ m and $X = 0.39$ m, corresponding to moderate and large vortex amplitudes, respectively. Overall, the velocity contours from the periodic solution match well with the corresponding contours from the original DNS solution. The agreement is very good within the inclined shear layer that bounds the crossflow vortex; however, some discrepancies may be noted in other parts of the vortex, particularly within the trough region of the contours at $X = 0.33$ m and the contours near the boundary layer edge on the left-hand side of the figure corresponding to $X = 0.39$ m.

B. Secondary instability characteristics

The procedure for instability analysis outlined in Sec. II was applied to the basic state described in Sec. III A. Three levels of analysis are used to understand the instability mechanisms driving the high-frequency secondary instabilities. As mentioned in Sec. II, a majority of the results are obtained using the equivalent of classical stability theory in the context of flows that are strongly inhomogeneous in two spatial directions, namely, a QPNC formulation. In general, the classical theory is the easiest to apply and to interpret in the context of new physical problems, especially a complex flow configuration such as the present one. It is also well established in the case of secondary instability analysis of subsonic and supersonic swept wing flows [59,60]. Thus, the QPNC results provide a convenient framework to describe the complex topology of secondary disturbances supported by the crossflow vortices over the cone, which represents a major contribution of the present study. Furthermore, the QPNC results provide the basis for a limited assessment of the effects of curvature (Sec. III B 2) and the combined effects of curvature and basic state nonparallelism (Sec. III B 3). The nonparallel predictions based on PSEs use the parallel results to provide initial disturbance profiles for the marching process. However, due to the cumulative effects of nonparallel terms, it can become challenging to classify the mode type at sufficiently downstream locations,

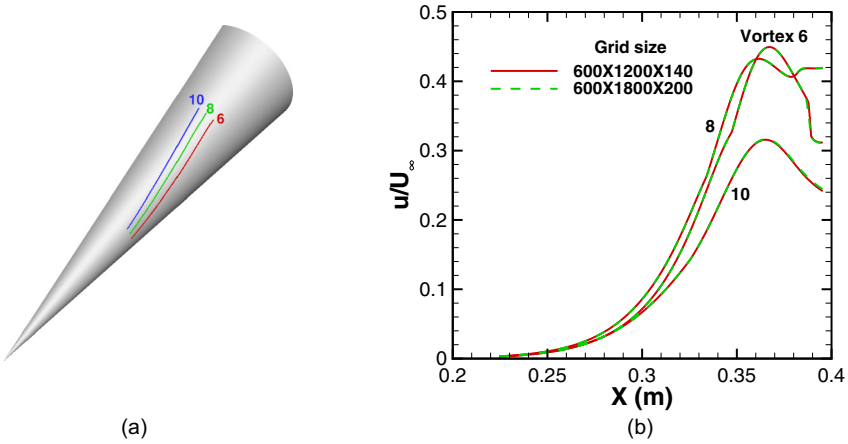

(a) (b)

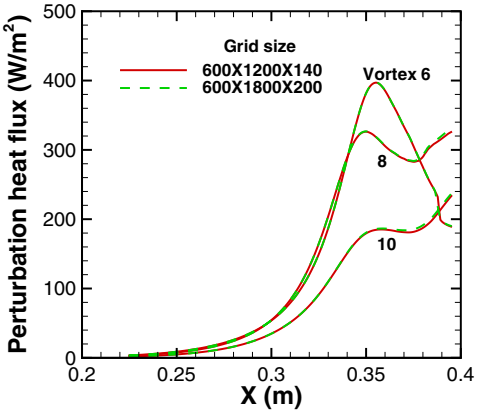

(c)

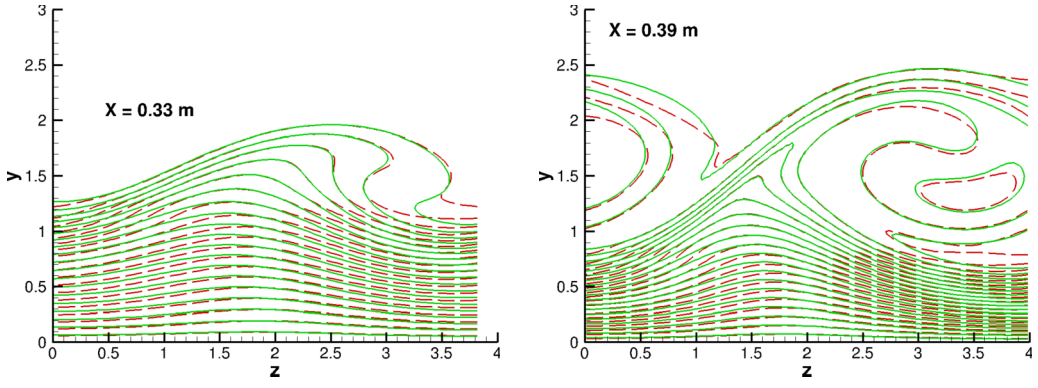

(d)

FIG. 4. Stationary crossflow vortices selected for secondary instability analysis: (a) selected vortex trajectories, (b) vortex amplitudes measured by peak axial velocity perturbation, (c) vortex amplitudes in terms of surface heat transfer, and (d) effect of imposing periodicity on basic state meridional velocity contours at $X = 0.33$ m (left) and $X = 0.39$ m (right); the dashed line shows the original solution and the solid line the periodic state, which is a total of 21 contours with a spacing of 5% of the maximum velocity at the location of interest.

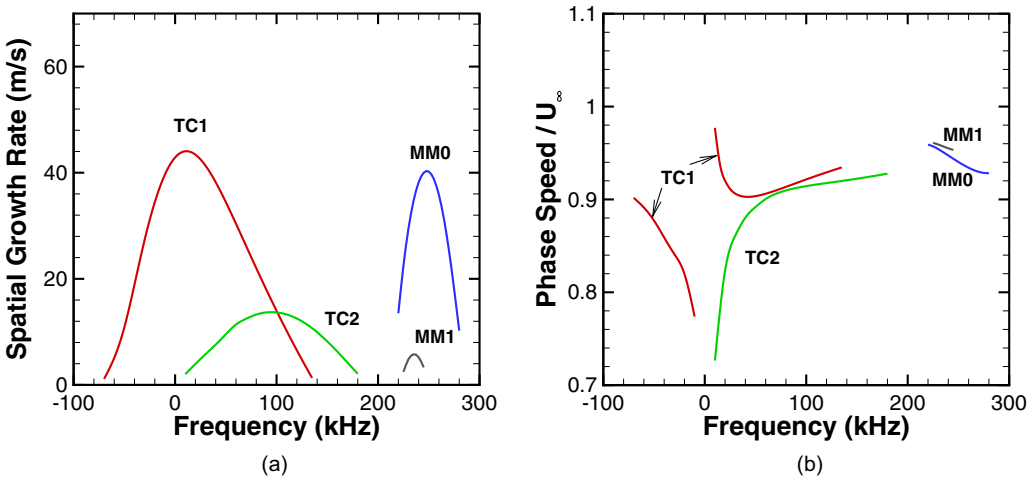

FIG. 5. Instability characteristics of vortex 10 as functions of frequency at an upstream station ($X = 0.25$ m): (a) growth rate spectra and (b) phase speed scaled by free-stream velocity.

especially in the presence of multiple instability mechanisms as described in Sec. III B 1. Thus, the parallel results continue to be useful by providing a reference to help interpret the PSE results.

1. Modal topology and quasiparallel predictions

A comprehensive analysis of secondary instability characteristics of multiple vortices is beyond the scope of this paper. Therefore, emphasis is placed on describing the secondary instabilities of a single vortex (chosen to be vortex 10) along with select features of two additional vortices (vortex 6 and vortex 8, respectively). Even though the peak amplitude of vortex 10 is somewhat smaller than that of vortex 6 and vortex 8, it adequately represents the modal characteristics of secondary disturbances and the overall amplification of the associated instability modes is comparable to that for the other two vortices. A representative spectrum of unstable modes for vortex 10 is shown in Fig. 5, wherein the spatial growth rate of dominant instabilities has been plotted as a function of frequency at $X = 0.25$ m. At $X = 0.25$ m, the amplitude of the primary crossflow vortex is relatively weak, so the predicted secondary instabilities are approximately equivalent to the primary instabilities of the unperturbed cone boundary layer with the additional constraint that the azimuthal wave number of the secondary mode be consistent with the local wavelength of the stationary vortex.

Figure 5(a) shows that the unstable disturbances at low amplitudes of the stationary crossflow vortex are concentrated in two separate frequency ranges. The low-frequency lobes (with peak frequencies below approximately 100 kHz) correspond to traveling crossflow instability modulated by the weak stationary crossflow vortex. Accordingly, they are labeled TC1 and TC2, respectively, where the numerical suffix identifies the index of the azimuthal harmonic corresponding to the stationary mode. Thus, the mode TC1 corresponds to one with an azimuthal wave number equal to the local fundamental wave number of the stationary vortex, whereas mode TC2 corresponds to one with an azimuthal wave number equal to twice the fundamental wave number. Similar to the primary crossflow instability, the modulated crossflow modes at the fundamental azimuthal wave number (mode TC1) include the zero-frequency mode that corresponds to the modulated analog of the stationary crossflow vortices. The negative-frequency modes simply represent the analytic continuation of the modulated crossflow modes beyond the stationary mode. Alternatively, the portion of the TC1 growth rate curve corresponding to negative frequencies could have been reflected across the $f = 0$ axis, indicating the positive-frequency segment of the complex conjugate counterpart of the mode denoted by TC1 in Fig. 5(a).

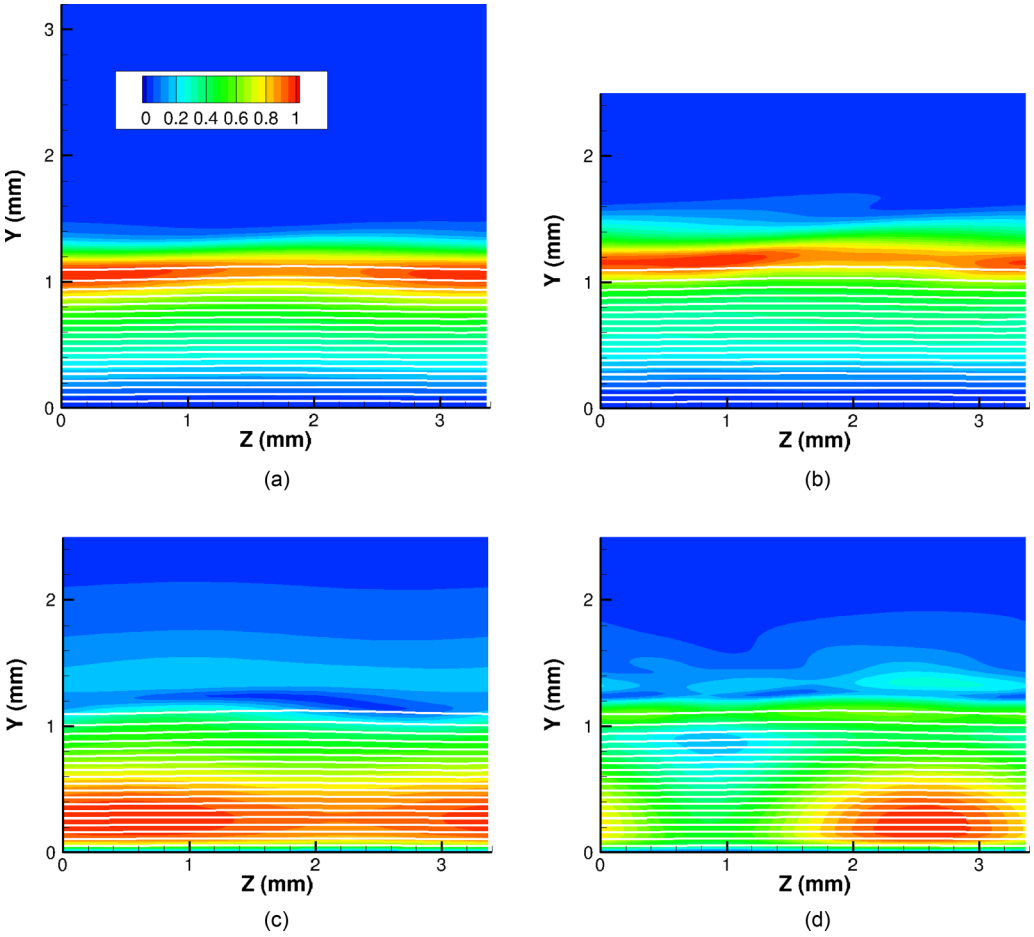

FIG. 6. Representative mode shapes for secondary disturbances from Fig. 5: (a) mode TC1 with $f = 14.5\,\text{kHz}$, (b) mode TC2 with $f = 93.3\,\text{kHz}$, (c) mode MM0 with $f = 245\,\text{kHz}$, and (d) mode MM1 with $f = 252\,\text{kHz}$. The coordinate Z denotes the azimuthal distance along the surface, whereas Y denotes the wall-normal distance from the cone surface. The parameter f denotes disturbance frequency. Basic state velocity contours are indicated via white lines.

The two high-frequency lobes in Fig. 5(a) correspond to second-mode (i.e., Mack mode) waves of the unperturbed boundary layer over the cone and hence have been labeled MM0 and MM1, respectively. The mode MM0 corresponds to the axisymmetric Mack mode, whereas mode MM1 corresponds to an oblique Mack mode with an azimuthal wave number equal to that of the stationary crossflow vortex. Because the growth rate of second-mode disturbances decreases rapidly with the wave angle, only the fundamental harmonic is unstable in this case. Over a majority of the frequency range shown in Fig. 5(b) (except for TC1 modes with very small frequencies), the phase speeds of all four modes fall within a narrow range of approximately 0.90–0.93 times the local edge velocity U_e in the axial direction. Representative mode shapes for the above families of disturbances are shown in Figs. 6(a)–6(d). For reference, these figures include the contours of meridional velocity associated with the basic state, which are indicated as white lines. The basic state contours are also included in all of the mode shapes presented in latter portions of this section. As shown in Fig. 6, peak velocity fluctuations associated with the Mack modes are relatively close to the surface, whereas those associated with the traveling crossflow modes are concentrated further away inside the boundary layer. In the remaining part of this paper, we focus mainly on the high-frequency disturbances, since

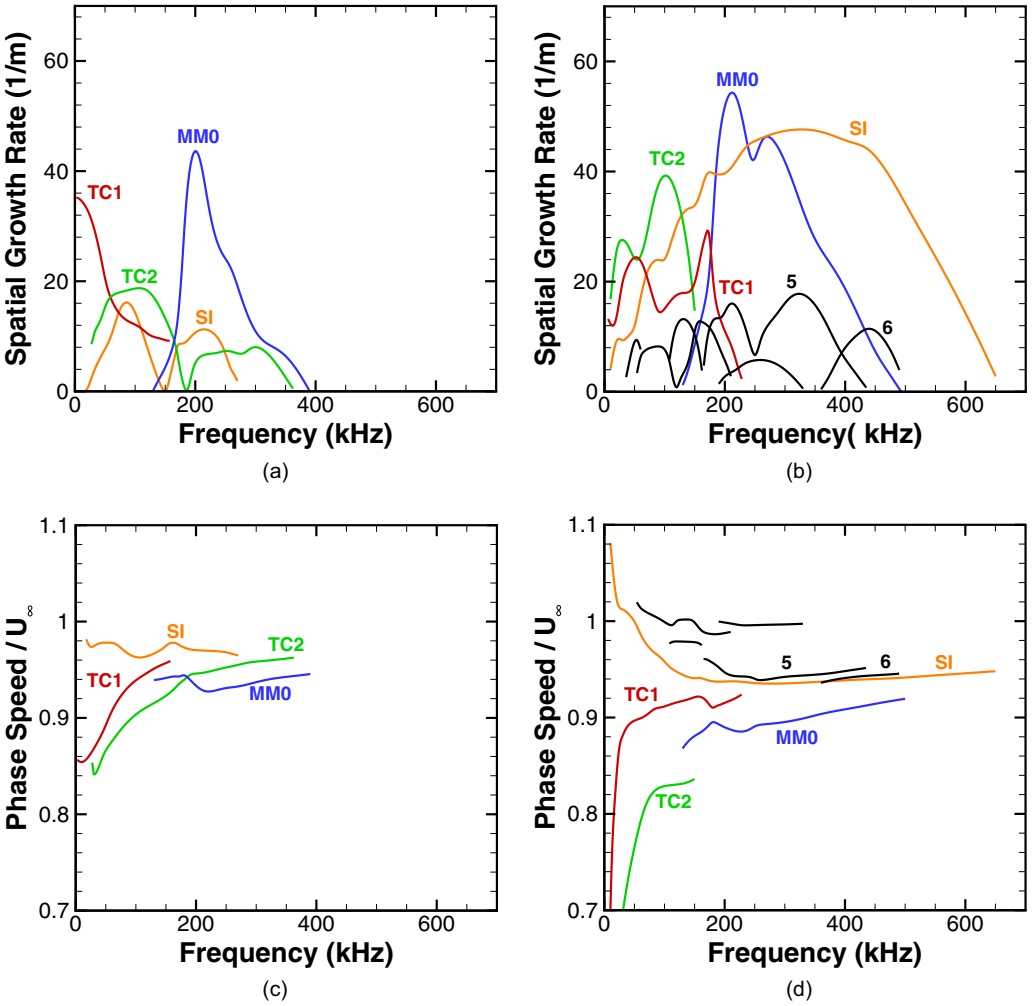

FIG. 7. Growth rate spectra at (a) $X = 0.30$ m and (b) $X = 0.33$ m and phase speed spectra at (c) $X = 0.30$ m and (d) $X = 0.33$ m for vortex 10 at selected downstream locations.

they appear to be linked more closely with the observed onset of laminar breakdown in the Purdue experiments [21,22].

The instability modes MM0, MM1, TC1, and TC2 discussed above are present even in the absence of the primary instability, i.e., the crossflow vortex, therefore, they are not, strictly speaking, true secondary instability modes. However, as will be shown, these modes are so strongly modulated by the growing crossflow vortices downstream that they bear very little resemblance to their respective unmodulated states that would otherwise exist in the absence of strong crossflow vortices. It is in this sense that these modes will herein be referred to as secondary instability in addition to the genuine secondary instability modes that will be discussed shortly.

As the amplitude of the stationary crossflow vortex increases in the downstream direction, the modal topology gets progressively modified and it becomes difficult to attribute a clear mode type to each family of unstable secondary disturbances, especially to the low-frequency modes, unlike that in Fig. 5. Hence, the unstable modes at downstream locations are denoted simply using a numerical index, ordered approximately in the order of decreasing peak-growth rate at the location of interest. A total of six dominant modes were selected for labeling in Fig. 7(a) at

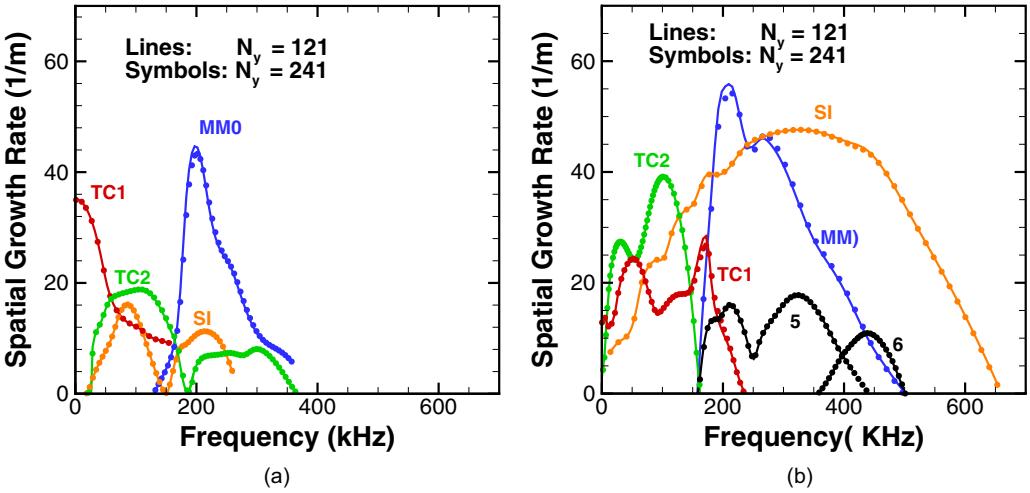

FIG. 8. Growth rate spectra derived from temporal theory for vortex 10 at the same locations as in Fig. 7: (a) $X = 0.30$ m and (b) $X = 0.33$ m. Results based on two different radial grids are shown using lines and symbols, respectively, to illustrate the lack of sensitivity to numerical resolution.

$X = 0.30$ m. Additional modes with relatively low peak-growth rates either are not labeled or have been omitted from the plot to minimize visual clutter. Similar results for instability characteristics at $X = 0.33$ m are shown in Fig. 7(b). The accuracy of these calculations was verified via temporal stability calculations on significantly different grids in both radial and azimuthal directions. As an illustration, Figs. 8(a) and 8(b) indicate the growth rate spectra at $X = 0.30$ and 0.33 m, respectively, that were obtained using both a typical grid of 121 points in the radial direction and a denser grid with the same distribution of grid spacing but twice the number of points. The temporal growth rate has been converted to an approximate spatial growth rate by scaling with the group velocity of the disturbance. As expected, there is perfect correspondence between the modal topologies based on the spatial (Fig. 7) and temporal (Fig. 8) theories. Furthermore, the close agreement between the actual spatial growth rates and those approximated via the temporal theory suggests that the temporal approximation could also have been used, if necessary, for the secondary instability analysis for the present flow configuration. A similar comparison to Fig. 8 was also obtained during spot checks involving even higher-order discretization in the radial direction (sixth-order versus the typical fourth-order discretization) and denser grids in the azimuthal direction. Representative mode shapes for the modes shown in Fig. 7(a) are plotted in Fig. 9.

Results at intermediate locations (not shown herein) suggested that the maximum growth rate of the oblique Mack mode (mode MM1 in Fig. 5) decreases with increasing X (and correspondingly, with a higher crossflow vortex amplitude). Therefore, at locations sufficiently far downstream, the only dominant high-frequency mode that is related to the Mack mode instabilities at upstream stations is a modified version of mode MM0 in Fig. 7(a). A comparison of the mode shapes in Figs. 6(c) and 9(b) indicates how the MM0 mode shape that was nearly uniform in the azimuthal direction at $X = 0.25$ m [Fig. 6(c)] becomes distorted at $X = 0.30$ m as a result of the increased amplitude of the stationary crossflow vortex. More important, the peak velocity fluctuations associated with the original MM0 mode were within the inner half of the boundary layer thickness; however, as a result of the interaction with the stationary vortex, the wall-normal location of peak fluctuations at $X = 0.30$ m has moved to the outer part of the boundary layer.

While mode MM1 from the upstream spectrum is no longer unstable at $X = 0.30$ m, Fig. 7(a) indicates the emergence of a new high-frequency mode (referred to as mode SI) that was not present at the upstream stations corresponding to low vortex amplitudes. At $X = 0.30$ m, the peak-growth rate of this new mode is substantially smaller than that of the modified MM0 mode. However, the

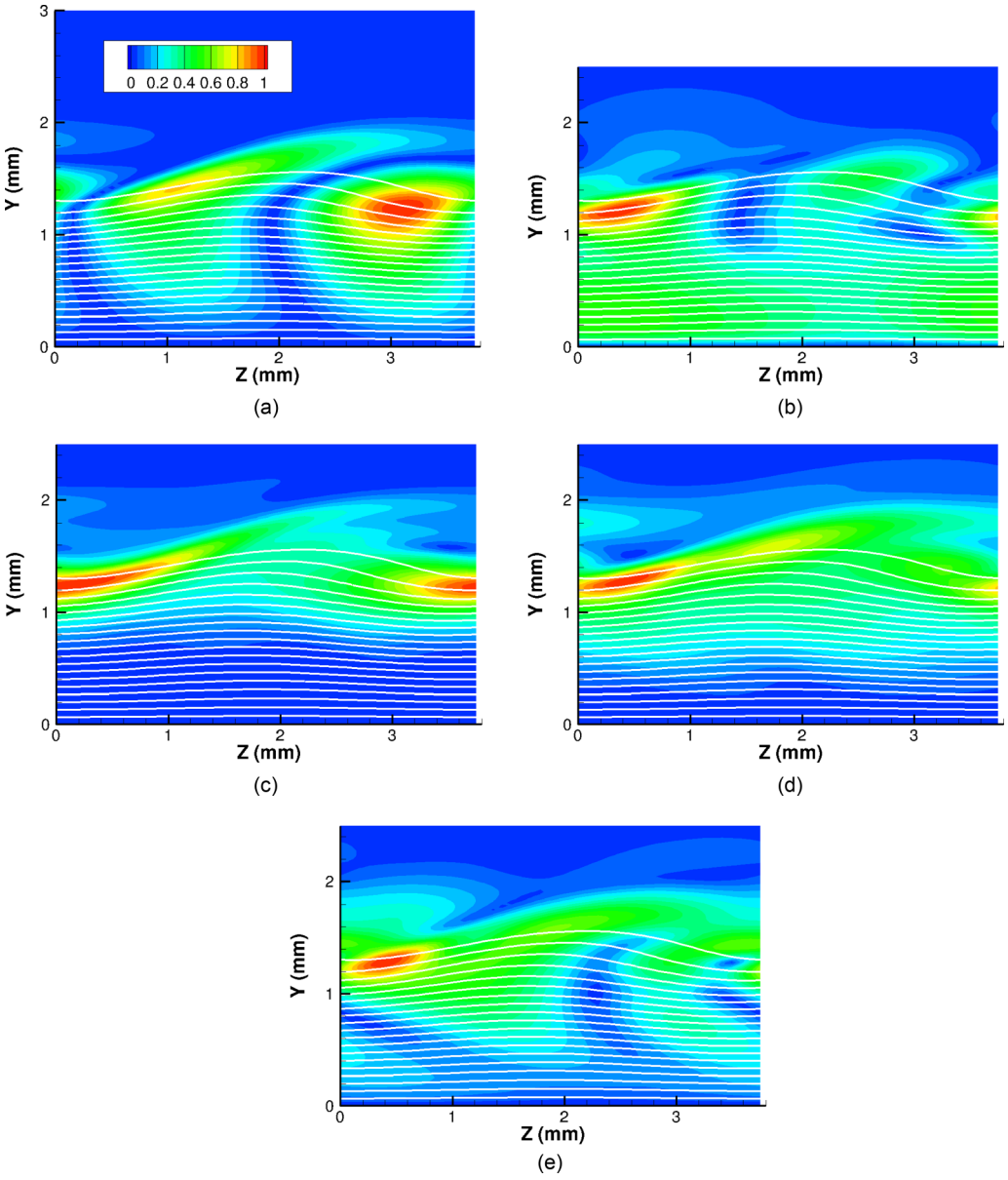

FIG. 9. Representative $|u'|$ mode shapes for secondary instabilities of vortex 10 at $X = 0.30$ m: (a) mode TC1 with $f = 111$ kHz, (b) mode MM0 with $f = 200$ kHz, (c) mode SI with $f = 213$ kHz, (d) mode TC2 with $f = 89$ kHz, and (e) mode TC2 with $f = 101$ kHz. Basic state velocity contours are indicated via white lines.

former increases rather rapidly with further amplification of the stationary crossflow vortex and hence approaches the peak-growth rate of the modified MM0 mode at $X = 0.33$ m [Fig. 7(b)]. The mode shape of the SI mode bears a remarkable resemblance to the secondary instability mode driven by the spanwise shear of the crossflow vortex in swept wing boundary layers [64,66]. Thus, the SI mode apparently represents a genuine secondary instability of the finite-amplitude crossflow vortex over the cone and hence the nomenclature assigned to this mode. A certain threshold amplitude of the stationary crossflow vortex is required for the onset of SI modes. Hence, they must originate from

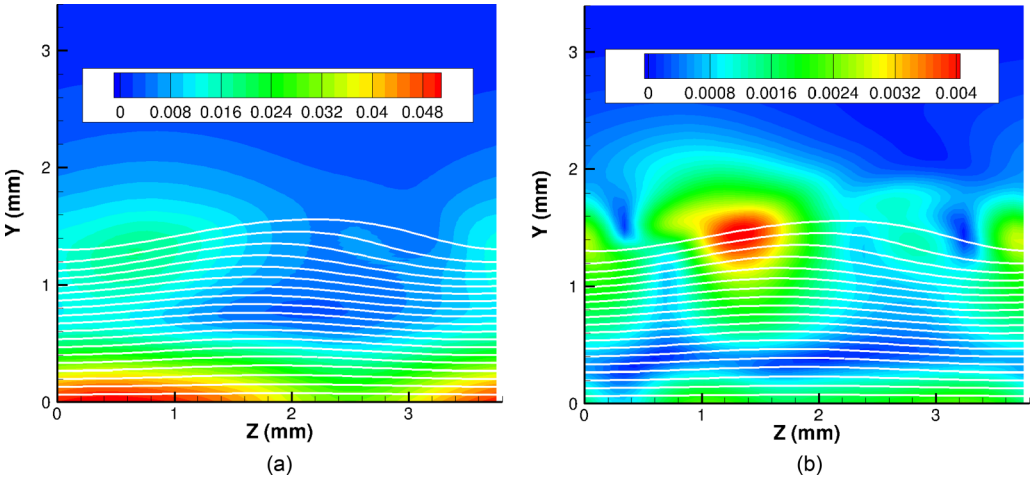

FIG. 10. $|p'|$ mode shapes for secondary disturbance types (a) MM0 with $f = 200\,\text{kHz}$ and (b) SI with $f = 218\,\text{kHz}$ ($X = 0.3\,\text{m}$). Basic state velocity contours are indicated via white lines.

a stable part of the spectrum at $X = 0.25\,\text{m}$ or, equivalently, from the spectrum of the unperturbed boundary layer in the absence of any crossflow vortices. The peak-growth frequency of the SI mode is even higher than that of the mode MM0 and the corresponding range of unstable frequencies at $X = 0.33\,\text{m}$ is significantly broader, extending from almost 0 kHz to over 600 kHz. The large frequency bandwidth of this mode appears consistent with its interpretation as an instability of the relatively thin, inclined shear layer associated with the overturning contours of axial velocity associated with a strong crossflow vortex [Fig. 3(b)].

Throughout the range of unstable frequencies, the phase speed of the SI mode is slightly higher than the phase speeds of other dominant modes (i.e., those originating from MM and TC instabilities of the unperturbed boundary layer) as depicted in Figs. 7(c) and 7(d). Figure 7(c) reveals a crossover between the phase speeds of modes MM0 and TC2 near 200 kHz, indicative of a local phase synchronization between those two modes. Such phase synchronization is interesting, because it would enable a local coupling between the two modes even within the framework of linear theory and hence is likely to influence the evolution of both modes. Such modal coalescence is not unusual in the context of streak instabilities. However, investigating the effects of this phase synchronization is beyond the scope of the present paper and it is left as a possible topic for future work.

Since the unsteady disturbance spectra in high-speed flows are often acquired via surface pressure transducers [20–23], the disturbance mode shapes for pressure fluctuation magnitudes for the MM0 and SI modes at $X = 0.30\,\text{m}$ are shown in Figs. 10(a) and 10(b), respectively. Analogous results for $X = 0.33\,\text{m}$ are plotted in Figs. 11(a) and 11(b). The figures show that the peak pressure fluctuations for the MM0 mode occur near the surface. In all cases, the $|p'|$ mode shapes are normalized such that the magnitude of the peak u' fluctuation across the cross section of the vortex is equal to unity. As expected, azimuthal variations in surface pressure amplitudes become more pronounced as the crossflow vortex amplitude increases from $X = 0.30\,\text{m}$ to $X = 0.33\,\text{m}$. The highest-pressure fluctuations associated with the SI modes are concentrated away from the surface, approximately at the same location as the peak velocity fluctuations. The peak surface pressure fluctuations at the surface are approximately two times weaker than those at the interior peak. In both cases, the azimuthal variation in the surface pressure fluctuation is relatively modest so that the sensitivity of measured $|p'|$ to the transducer location is expected to be small.

The cumulative growth characteristics for the most unstable MM0 and SI modes are considered next. Figure 12(a) shows the variation of the logarithmic amplification ratio, i.e., N factor, along the cone length for selected frequencies of vortex 10 instabilities. Corresponding results for vortex 6

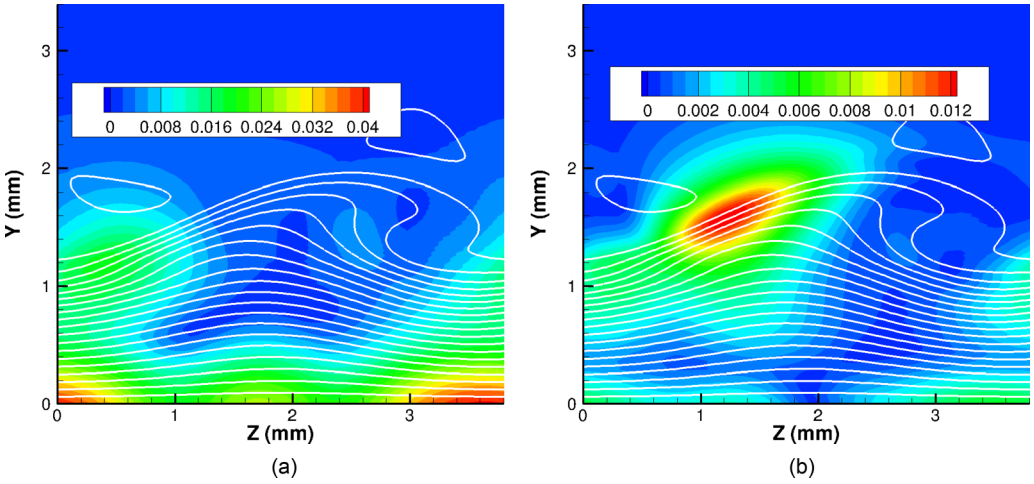

FIG. 11. $|p'|$ mode shapes for secondary disturbance types (a) MM0 with $f = 213\,\text{kHz}$ and (b) SI with $f = 340\,\text{kHz}$ ($X = 0.33\,\text{m}$). Basic state velocity contours are indicated via white lines.

are shown in Fig. 12(b). Each solid curve denotes a fixed-frequency MM0 mode, whereas the dashed curves denote the SI modes. The N factor is defined as the natural logarithm of the ratio of the disturbance amplitude at the station of interest relative to that at a suitable reference location upstream. In general, the reference location corresponds to the station where a given disturbance first becomes unstable. However, in the present case, the crossflow vortex is only defined starting slightly downstream of the roughness elements (i.e., near $X = 0.18\,\text{m}$). For disturbances that are already unstable at this location (i.e., their neutral station is upstream of the region of stationary vortices), the reference location is chosen to be $X = 0.18\,\text{m}$. In effect, the source of secondary disturbances is also assumed to coincide with the source location for the primary crossflow vortices. If the source of unsteady fluctuations were to be upstream of this location, some of the frequencies associated with the MM disturbances would achieve higher N factors than those presented here. However, because of the relatively weak growth of those disturbances in the unperturbed boundary layer, the resulting correction to the N factors would still be small, estimated to be less than $\Delta N = 1$.

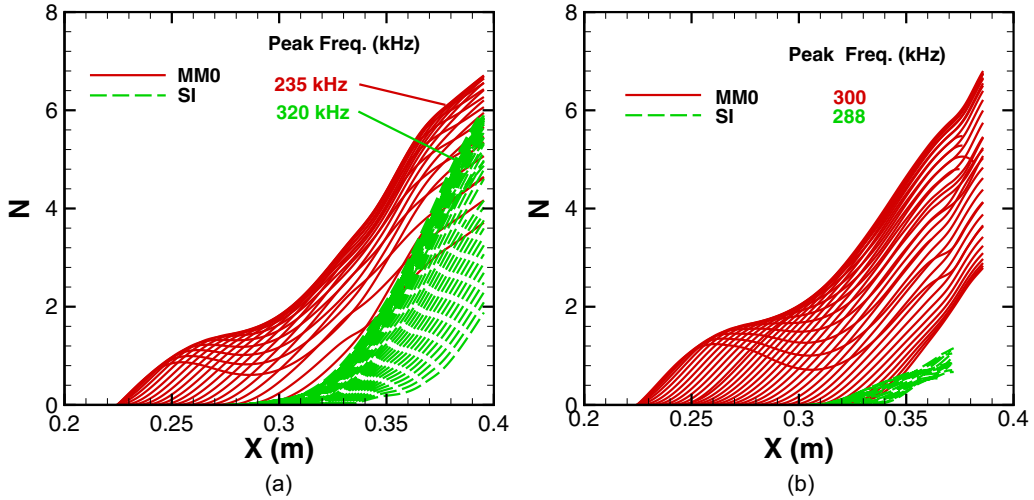

FIG. 12. N-factor evolution along (a) vortex 10 and (b) vortex 6 using quasiparallel, no-curvature theory.

For vortex 10, the most amplified MM0 mode has a frequency of approximately 235 kHz, whereas the peak frequency of the SI mode is significantly higher, being equal to 320 kHz. The N-factor curves in Fig. 12(a) imply that the MM0 modes of vortex 10 begin to amplify when the stationary crossflow modes are still very weak. Consistent with typical second- (i.e., Mack) mode behavior, the growth rates begin to decrease within a relatively short distance after their onset (as indicated by the decreasing slopes of the N-factor curves leading to a local plateau in the envelope between approximately $X = 0.25$ and 0.3 m) and then increase again as the amplitude of the stationary crossflow vortex increases sufficiently (as reflected in the renewed rise in the N-factor envelope following the plateau). For some of the disturbance frequencies, the renewed increase in N factors is preceded by a modest decay in the amplitude of the MM0 mode. In general, the second region of rising N factors accounts for a majority of the overall amplification contributing to the peak-N-factor values over the length of the cone. In the absence of the stationary crossflow vortex, the maximum N factors of second-mode disturbances would remain below $N = 2$. The substantial increase in N factors of the MM0 modes in the region of high crossflow amplitudes illustrates the dramatic effect of the modulation of the MM0 mode by the large-amplitude crossflow vortex. In contrast to the MM0 modes that can exist in the absence of the stationary crossflow vortices (albeit with substantially lower amplification potential), the onset of the SI modes occurs only after the amplitude of the crossflow vortex has become sufficiently large. The range of threshold crossflow amplitudes near the onset of SI modes corresponds to approximately 5%–10% in terms of the peak axial velocity perturbation scaled by the freestream speed.

For vortex 10, the onset of SI modes approximately coincides with the start of the second region of MM0 mode amplification. In the range of approximately $X = 0.35$–0.40 m (where vortex 10 has its largest amplitudes), the peak-growth rates of the SI mode are larger than the peak-growth rates of the MM0 mode as indicated by the relative slopes of the corresponding N-factor curves. However, the peak N factor of the SI modes at the end of the 0.40-m length of the Purdue cone remains slightly smaller than the peak N factor associated with the modified Mack modes. The N-factor differential between the two modes is approximately equal to one. The reader may also recall from Figs. 9 and 10 that the mode MM0 has a stronger signature at the surface than the SI mode.

Compared to vortex 10, the growth of SI modes for vortex 6 begins farther downstream [where the crossflow amplitudes are $O(10\%)$, nearly twice the value corresponding to vortex 10] and the peak-growth rates remain smaller. Consequently, the overall growth of the high-frequency disturbances over vortex 6 is entirely dominated by the MM0 mode. The reasons behind the lower-N factors of SI modes of vortex 6 are not entirely clear. They might be related to the larger spanwise wavelength of the crossflow vortices farther away from the leeward plane (since a larger wavelength would imply weaker azimuthal gradients of the basic state to facilitate energy transfer to the secondary instabilities). The maximum SI mode N factor for vortex 8 is in between the N-factor values for vortices 6 and 10, confirming a gradual variation in SI mode amplification along the azimuthal direction [Fig. 11(c)].

Mode shape evolution for the MM0 and SI modes of vortex 10 with the highest amplification ratios is shown in Fig. 13. The evolution of velocity disturbances associated with the MM0 mode indicates how the peak fluctuations rise above the surface with increasing downstream distance. At the farthest downstream locations ($X = 0.35$ and 0.375 m), where the amplitude of the stationary crossflow vortex is large, the MM0 fluctuations are concentrated in the high shear layer corresponding to the troughs of the velocity contours associated with the primary vortex. On the other hand, the mode shape of the SI mode remains very similar throughout the evolution of this mode and is concentrated along the inclined portion of the high shear layer bounding the stationary crossflow vortex as mentioned previously.

A comparison of the results plotted in Figs. 12(a) and 12(b) shows that the peak frequency of MM0 mode decreases from vortex 6 to vortex 10 because of the increase in boundary layer thickness from windward to leeward planes. On the other hand, the frequency of the SI mode is strongly influenced by the characteristics of the inclined shear layer, which are determined by the wavelength and amplitude of the stationary crossflow vortex. Thus, in fact, one finds that the peak disturbance

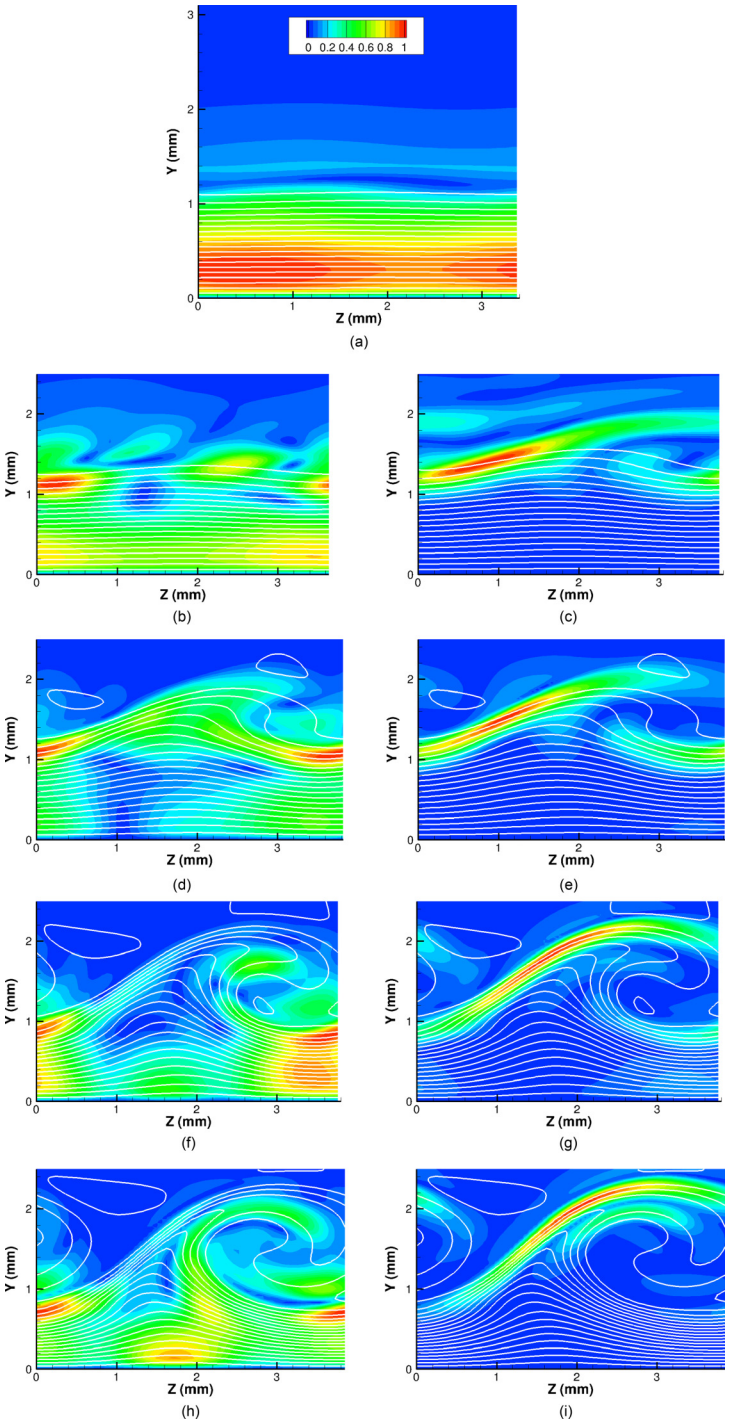

FIG. 13. Streamwise evolution of $|u'|$ mode shapes for dominant instabilities of vortex 10 ($f = 235$ kHz for mode MM0 and $f = 320$ kHz for mode SI): (a) mode MM0 with $X = 0.25$ m, (b) mode MM0 with $X = 0.28$ m, (c) mode SI with $X = 0.30$ m, (d) mode MM0 with $X = 0.325$ m, (e) mode SI with $X = 0.325$ m, (f) mode MM0 with $X = 0.35$ m, (g) mode SI with $X = 0.35$ m, (h) mode MM0 with $X = 0.375$ m, and (i) mode SI with $X = 0.375$ m. Basic state velocity contours are indicated via white lines.

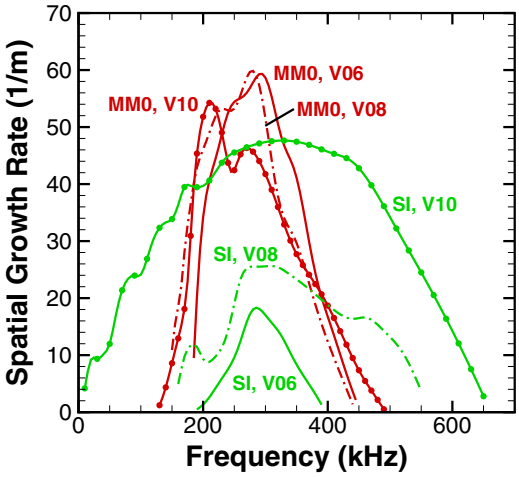

FIG. 14. Variation in growth rate spectra along azimuthal direction ($X = 0.33$ m). The curves denoted by V06, V08, and V10 indicate the growth rate variations for vortices 6, 8, and 10, respectively.

frequency of the SI mode as predicted via the quasiparallel stability theory employed herein increases from vortex 6 to vortex 10.

Figure 14 shows the azimuthal variation in growth rate spectra for modes MM0 at $X = 0.33$ m. In particular, growth rate spectra for vortices 6, 8, and 10 are shown as functions of the disturbance frequency. The peak frequency of the MM0 modes is the highest for vortex 6 and lowest for vortex 10. This variation in peak frequency is qualitatively consistent with the accompanying increase in underlying boundary layer thickness from windward to leeward planes. Unlike the MM0 modes, the peak frequency of the SI modes does not show any pronounced variation from vortex 6 to vortex 8, probably because the frequency of SI modes is influenced by the characteristics of the inclined shear layer near the boundary of the crossflow vortex structure and these characteristics are determined by the amplitude and the azimuthal wavelength of the crossflow vortex. On the other hand, unlike the amplification rates of MM0 modes, the peak-growth rate of the SI modes increases substantially from vortex 6 to vortex 10, in spite of the fact that the peak velocity amplitude of vortex 10 at $X = 0.33$ m is lower than the amplitudes of the other two vortices. The variation in growth rate may be related to the smaller azimuthal wavelength of vortex 10, which implies potentially stronger azimuthal gradients in the basic state that drive this particular mode of secondary instability.

2. Effects of transverse surface curvature

The quasiparallel predictions from Sec. III B 1 can be easily extended by including terms that correspond to the effect of the transverse curvature of the cone surface. Growth rate spectra with and without curvature at two representative locations are shown in Figs. 15(a) and 15(b), respectively. At $X = 0.25$ m [Fig. 15(a)], where the stationary crossflow amplitudes are relatively small, the convex transverse curvature is stabilizing for both low- and high-frequency modes. The curvature-related correction to the peak growth is larger for the dominant traveling crossflow mode in comparison with that for the MM0 mode. The frequency range of unstable disturbances also becomes slightly smaller when the curvature effects are considered. The effect of transverse curvature on the instability growth rates is reversed at larger amplitudes of the stationary crossflow vortex [Fig. 15(b) for $X = 0.33$ m]. The overall growth rates are now larger in the presence of the curvature terms and the frequency bandwidth of MM0 modes shows a significant increase, especially at the upper end of the frequency range of unstable disturbances. At larger crossflow amplitudes, the SI modes also come into play as described previously. However, the effect of curvature is somewhat stronger in the case of the MM0

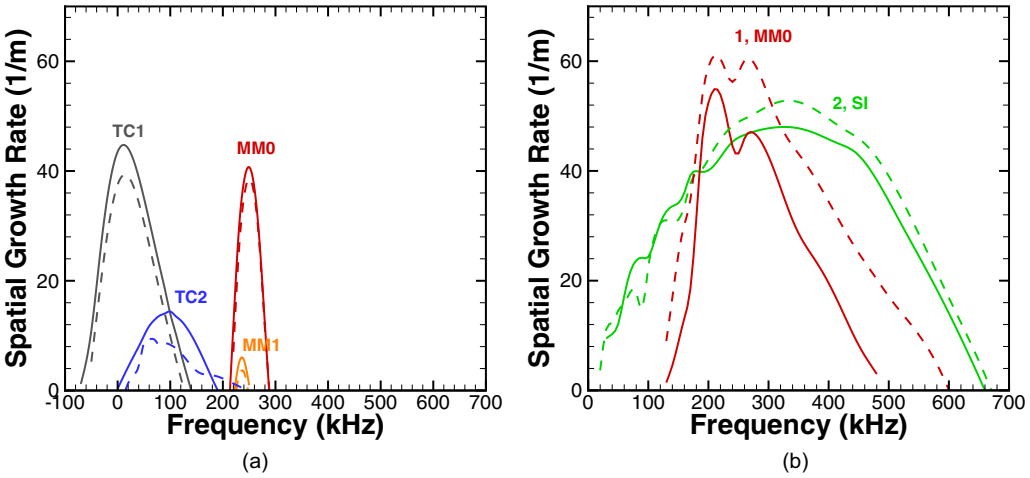

FIG. 15. Effect of transverse curvature on growth rate spectra corresponding to relevant instability modes of vortex 10 [only dominant high-frequency modes are included in (b)]: (a) $X = 0.25$ m and (b) $X = 0.33$ m. Solid lines indicate quasiparallel with no curvature and dashed lines quasiparallel with curvature.

modes. Whereas the inclusion of transverse curvature increases the peak-growth rates corresponding to the two maxima in the MM0 curve by 11% and 29%, respectively, the peak-growth rate of the SI modes is increased by approximately 10%. As the SI modes are much more localized and the peak fluctuations occur somewhat away from the surface, the effect of surface curvature on the growth rates of the SI modes is weaker than that in the case of the MM0 modes. Because the curvature-induced destabilization of the MM0 modes is greater than the weak stabilizing correction at the upstream stations, the effect of curvature terms on the overall amplification of MM0 modes is expected to be destabilizing. The growth rates based on the disturbance kinetic energy can be calculated from the X derivative of the N_K curves. The inclusion of nonparallel effects leads to higher growth rates than those based on the quasiparallel theory with curvature terms. For the dominant MM0 mode with a frequency of 260 kHz, the increase in amplification rate is 54% at $X = 0.33$ m and 23% at $X = 0.36$ m, whereas for the most amplified SI mode with $f = 360$ kHz, the nonparallel amplification rate is higher by 22% at $X = 0.33$ m and by 27% at $X = 0.36$ m.

The curvature-induced changes in the growth rates of secondary disturbances at the downstream station, i.e., in the presence of large-amplitude crossflow vortices, prompt an examination of curvature effects on the structure of the high-frequency secondary modes. Mode shapes corresponding to the magnitude of u' velocity fluctuation for an MM0 mode with $f = 260$ kHz are shown in Fig. 16. Similar to Fig. 13(b), the MM0 mode shape at $X = 0.28$ m [Fig. 16(a)] indicates an outward radial shift in the peak $|u'|$ location at upstream stations. As the stationary crossflow vortex approaches its peak amplitude just downstream of $X = 0.35$ m, the peak velocity fluctuations become concentrated along the inclined shear layer that bounds the velocity contours associated with the stationary vortex [Fig. 16(b)]. This mode shape is rather different from the distribution of $|u'|$ in the absence of any curvature effects [Fig. 14(f)] and in fact is quite similar to the mode shape of the SI mode driven by the azimuthal gradients of the basic state [Fig. 13(g)]. The effect of transverse curvature on the mode shape is rather surprising. The presence of curvature does alter the relative orientation of the vortex trajectory from windward side of the stationary vortex to its leeward side. However, whether or not this nonuniform orientation would cause the peak fluctuations to rise from the valley region to the inclined part of the shear layer is not clear at this stage. Although not shown, the presence of transverse curvature does not have a major influence on the mode shape of the SI modes, which remain similar to the prediction without any curvature effects in Fig. 13(g).

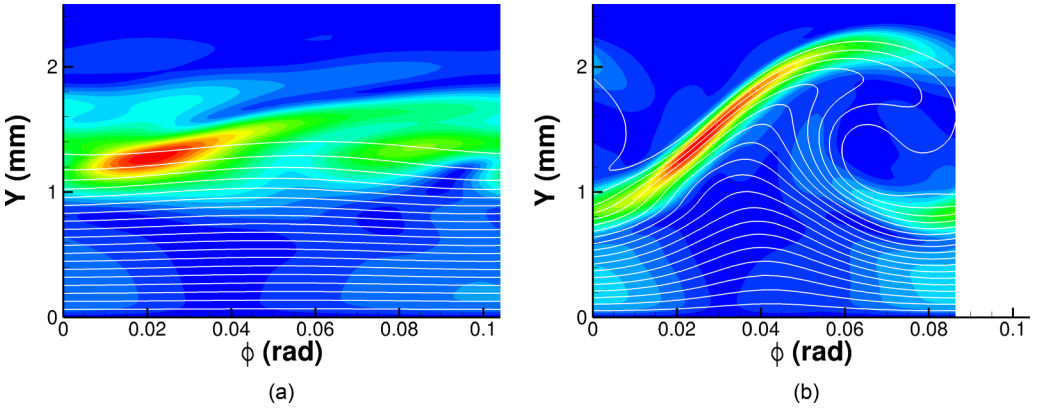

FIG. 16. $|u'|$ mode shapes for the MM0 mode of vortex 10 ($f = 260$ kHz): (a) $X = 0.28$ m and (b) $X = 0.35$ m; ϕ denotes the azimuthal coordinate in radians and the horizontal extent of each figure corresponds to the wavelength of the stationary vortex. Basic state velocity contours are indicated via white lines.

3. Combined effects of transverse surface curvature and nonparallelism

The quasiparallel predictions discussed in Secs. III B 1 and III B 2 do not account for the effects of basic state evolution along the vortex trajectory. The effects of changes in both the unperturbed boundary layer over the cone and the associated evolution of the stationary crossflow vortex are accounted for by using the plane marching PSE, which also includes the effects of transverse curvature. The resulting evolution of N-factor curves for fixed-frequency disturbances corresponding to the MM0 mode and the most amplified SI mode of vortex 10 is shown in Fig. 17. The frequencies of the most amplified MM0 modes (≈260 kHz) and SI modes (≈360 kHz) as predicted on the basis of PSE are slightly larger than the predictions of the quasiparallel theory (approximately 235 and 320 kHz, respectively). This difference is not large in our opinion, but it will be significant if it happens to result in a substantially narrower gap with future measurements that involve a similar

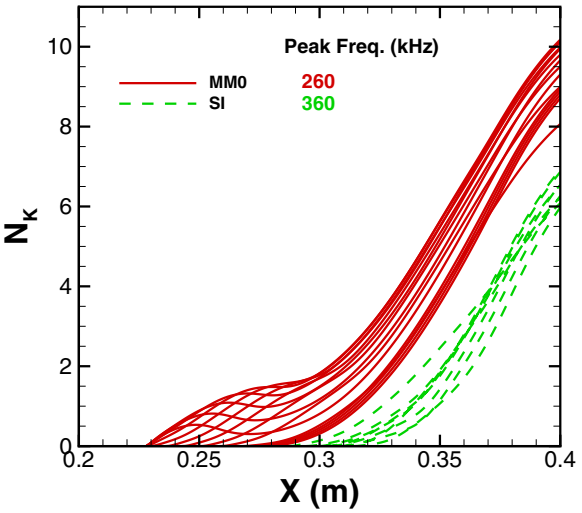

FIG. 17. N-factor evolution along vortex 10 using plane marching PSEs (N_K denotes the N factor based on disturbance kinetic energy integrated along the azimuthal and wall-normal directions). Curve legends indicate the frequency of the dominant mode reaching the highest N factor within each family of modes.

excitation of stationary crossflow modes as in the present DNS. The overall slopes of N-factor curves for both mode types in Fig. 17 are quite similar within the region of SI modes, indicating that the growth rates of both modes are comparable to each other when the stationary crossflow amplitude is sufficiently large. The similarity in growth rates is not surprising in view of the facts that the peak-growth frequencies of both modes are relatively close and, as shown later, the associated mode shapes have peak fluctuations within a common region corresponding to the shear layer that bounds the crossflow vortex structure. Because of the earlier onset of the MM0 modes where the amplitude of vortex 10 is too small to induce significantly unstable SI modes, the peak N factors of MM0 modes are consistently higher than those of the SI modes. The difference between the peak N factors of the two modes approximately corresponds to the amplification achieved by the MM0 modes until the stationary crossflow amplitudes have become large enough to induce further growth of those modes. The overall difference in PSE-based N factors of the MM0 and SI modes near the end of the computational domain is similar to that predicted in Fig. 12 by using the QPNC theory. Such similarity suggests that the quasiparallel theory may capture the broad trends in amplification characteristics reasonably well, but that the refined computations using PSEs may become necessary to make more accurate predictions of disturbance growth rates and amplification factors. However, because this paper represents an application of either technique to high-frequency secondary instabilities of crossflow vortices at a hypersonic Mach number, higher-fidelity data derived from either DNS or experimental measurements will be necessary to confirm the relative accuracy of the quasiparallel and PSE techniques.

The PSE-based mode shapes for $|u'|$ from Fig. 18 are discussed next. The MM0 mode shapes in the presence of a strong stationary vortex (i.e., $X \geqslant 0.325$ m) are similar to the QPWC prediction in Fig. 16(b), indicating that the nonparallel terms primarily influence the growth rates of the high-frequency secondary modes. One noticeable difference in mode shapes corresponds to the $X = 0.28$ m location, where the PSE-based MM0 mode shape in Fig. 18(b) still has its peak fluctuations near the surface. However, because the location of peak fluctuations eventually rises well above the surface, the nonparallel terms appear to simply delay that rise but not prevent it. Similar to the QPWC predictions, the mode shapes of the SI modes are concentrated along the inclined shear layer and hence are similar to the mode shapes of MM0 modes in the region of large crossflow amplitudes.

Analogous to the $|u'|$ mode shapes in the region of high crossflow amplitude (i.e., $X \geqslant 0.325$ m in Fig. 18), the $|p'|$ mode shapes of the MM0 and SI modes (Fig. 19) also indicate a peak within the inclined shear layer associated with the stationary crossflow vortex. However, relative to the $|u'|$ mode shapes, the $|p'|$ mode shapes from the MM0 and SI families remain somewhat distinct from each other. Throughout the streamwise region of interest, the overall maximum of the $|p'|$ fluctuations associated with the MM0 modes is located at or near the wall, whereas the highest $|p'|$ fluctuations induced by the SI modes occur away from the surface. Of course, experimental measurements of the $|p'|$ fluctuations are usually limited to the surface, where the SI modes still induce a finite pressure disturbance. Consequently, differences, if any, between the wall-normal structure of pressure fluctuations associated with the secondary modes are not likely to be detected in the experiments.

As discussed in the context of Fig. 17, the earlier onset of the MM0 modes contributes to higher amplification ratios than those of the SI modes. The N-factor curves based on PSE computations of MM0 modes of vortex 8 and vortex 6 are shown in Figs. 20(a) and 20(b), respectively. The peak N factor for vortex 8 in Fig. 20(a) is very close to that for vortex 10 in Fig. 17; however, the peak N factor for vortex 6 is moderately lower, as shown in Fig. 20(b), indicating that the N-factor values for secondary disturbances are not necessarily proportional to the peak amplitude of the stationary vortex. Similar to the QPNC predictions presented earlier, the frequency of the most amplified MM0 mode increases slowly from vortex 10 to vortex 6. This increase in dominant frequency is consistent with the fact that the thickness of the unperturbed boundary layer increases from the windward to the leeward direction (i.e., with increasing vortex number) and the Mack mode frequencies are known to correlate with the boundary layer thickness in general. The computational results from Figs. 17

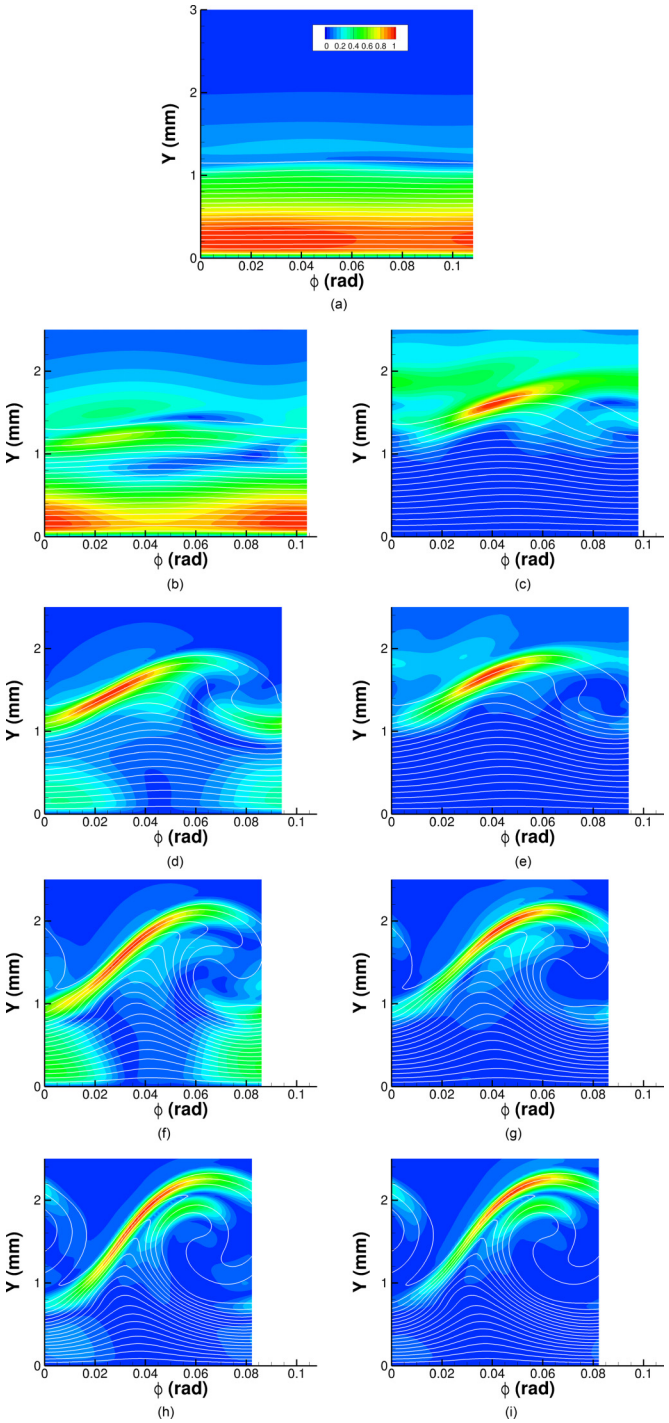

FIG. 18. Streamwise evolution of PSE predictions of $|u'|$ mode shapes for dominant instabilities of vortex 10 ($f = 260\,\text{kHz}$ for mode MM0 and $f = 360\,\text{kHz}$ for mode SI): (a) mode MM0 with $X = 0.25\,\text{m}$, (b) mode MM0 with $X = 0.28\,\text{m}$, (c) mode SI with $X = 0.31\,\text{m}$, (d) mode MM0 with $X = 0.325\,\text{m}$, (e) mode SI with $X = 0.325\,\text{m}$, (f) mode MM0 with $X = 0.35\,\text{m}$, (g) mode SI with $X = 0.35\,\text{m}$, (h) mode MM0 with $X = 0.375\,\text{m}$, and (i) mode SI with $X = 0.375\,\text{m}$. Basic state velocity contours are indicated via white lines.

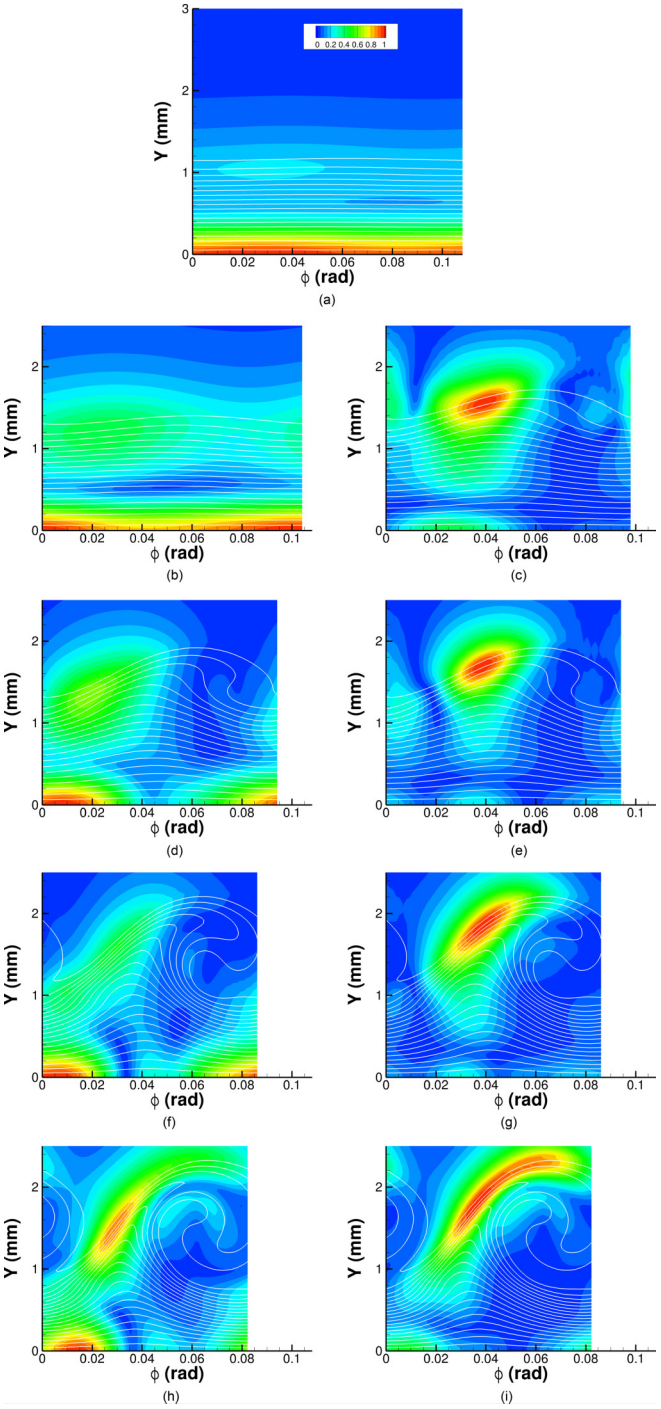

FIG. 19. Streamwise evolution of PSE predictions of $|p'|$ mode shapes for dominant instabilities of vortex 10 ($f = 260\,\text{kHz}$ for mode MM0 and $f = 360\,\text{kHz}$ for mode SI): (a) mode MM0 with $X = 0.25\,\text{m}$, (b) mode MM0 with $X = 0.28\,\text{m}$, (c) mode SI with $X = 0.31\,\text{m}$, (d) mode MM0 with $X = 0.325\,\text{m}$, (e) mode SI with $X = 0.325\,\text{m}$, (f) mode MM0 with $X = 0.35\,\text{m}$, (g) mode SI with $X = 0.35\,\text{m}$, (h) mode MM0 with $X = 0.375\,\text{m}$, and (i) mode SI with $X = 0.375\,\text{m}$. Basic state velocity contours are indicated via white lines.

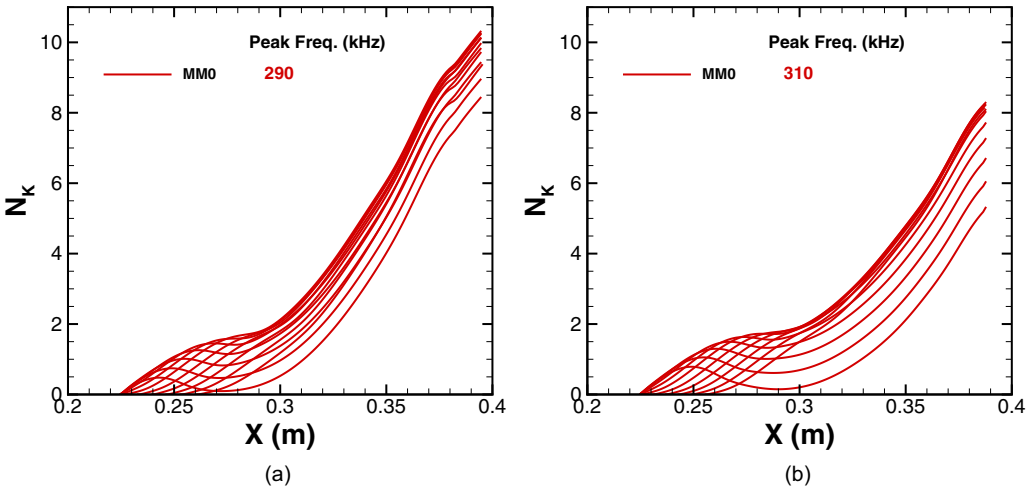

FIG. 20. N-factor evolution along (a) vortex 8 and (b) vortex 6 using plane marching PSEs (N_K denotes the N-factor based on the disturbance kinetic energy integrated along the azimuthal and wall-normal directions). The frequency of the disturbance mode reaching the highest N factor is indicated by the legend.

and 20 indicate that the strong spanwise distortion of MM0 fluctuations by the stationary crossflow structure does not destroy the latter correlation.

Experiments [67] and computations [68–73] of crossflow breakdown in subsonic swept wing boundary layers have shown that the high-frequency secondary instabilities can be rapidly amplifed by orders of magnitude to initiate the onset of transition. The N factors of both MM0 and dominant SI modes in the present hypersonic case are also large enough to enable these modes to reach nonlinear levels and induce the onset of transition when excited via a suitable disturbance environment. The presence of the additional MM0 modes that were absent from the subsonic case opens up the possibility of a new breakdown mechanism in the hypersonic case. Thus, future computations of nonlinear interactions involving the broader set of high-frequency modes would be of great interest.

IV. CONCLUSION

The present analysis of high-frequency instabilities of finite-amplitude crossflow vortices over a yawed circular cone in a Mach 6 free stream has identified and described the complex topology of secondary disturbances in this flow configuration, including a limited assessment of the effects of surface curvature and basic state nonparallelism on the modal evolution. The results reveal fundamental differences from the previous studies of secondary instability in subsonic and low supersonic Mach numbers. The lower-speed flows exhibited a clear separation between the frequency range of primary nonstationary modes of the unperturbed boundary layer and the dominant high-frequency secondary modes of the stationary crossflow vortices. In contrast, the high-frequency secondary instability modes of crossflow vortices at Mach 6 have frequencies comparable to those of the Mack mode instabilities in the unperturbed boundary layer without any crossflow vortices. This leads to a more complex topology of unstable secondary modes with possible interconnections as divulged by the modal crossover encountered during the numerical computations.

The other major difference between the present investigation and the past studies for lower-speed flows is related to the flow geometry. The infinite swept wing configurations targeted in the prior studies led to a spanwise periodic pattern of crossflow vortices that enabled a rigorous formulation of spatial instability theory [59,60]. On the other hand, the azimuthally inhomogeneous nature of crossflow instability over a cone required further approximations to make the secondary instability analysis tractable via similar methodologies, namely, the 2D, partial-differential-equation-based

eigenvalue analysis and plane marching parabolized stability equations. The present analysis isolated individual vortex structures from the quasiperiodic pattern over the cone and rendered each of them periodic in the azimuthal direction. Even though the simplifying approximations employed in the present work seem physically reasonable, they are not unique and a further assessment of those approximations would be a useful topic for future investigations.

In addition to clarifying the topology of unstable disturbances, the analysis in this paper has led to useful insight into existing experimental observations. This was achieved by exciting a pattern of stationary crossflow vortices that resembles the measured spacing, amplitudes, and velocity contours of crossflow vortices on the experimental models. Quiet tunnel experiments at Purdue University [21] have detected high-frequency disturbances in the range of 125 kHz and above during an apparent breakdown of large-amplitude stationary crossflow vortices on a yawed circular cone in the Mach 6 BAMQT facility at Purdue University. The observed dependence of these high-frequency disturbances on a threshold stationary wave amplitude and their localized azimuthal signature led these investigators to suggest that these disturbances were caused by the secondary instability of the stationary crossflow modes. In contrast, Munoz *et al.* [20] attributed the high-frequency measurements in a conventional facility to second-mode waves. The instability analysis in this paper has shown that the high-frequency disturbances may be attributed to both second-mode waves modified by finite-amplitude crossflow vortices and a genuine secondary instability of the stationary vortices.

At sufficiently high stationary crossflow amplitudes, the original second-mode (i.e., Mack mode) disturbances are further destabilized, resulting in peak-growth rates that are significantly larger than those of second-mode disturbances in the absence of any crossflow vortices. Large-amplitude crossflow vortices also lead to additional instability modes that originate from the stable part of the spectrum at low vortex amplitudes. In other words, these instabilities require a threshold crossflow amplitude in order to be amplified and hence they represent genuine secondary instabilities due to azimuthal modulation of the boundary layer by the primary crossflow vortices. In the cases studied, only one of these modes (referred to as the SI mode herein) had large enough growth rates to achieve comparable N factors to Mack mode disturbances. Unlike the Mack mode disturbances, the SI mode was found to be unstable over a broad range of frequencies and its mode shapes are similar to the known class of secondary instabilities in subsonic swept wing boundary layers that is driven by energy production mechanisms associated with spanwise (or azimuthal) basic state shear. Yet the frequencies of the most amplified modified Mack modes and the SI mode are both in the range of 200–360 kHz, with noticeable variation depending on the location of interest and the amplitude of the crossflow vortex. The above frequency range is approximately consistent with the frequencies measured in the experiments at Purdue University [21–23] and the Technical University of Braunschweig [20]. The present computations have also shown that both types of high-frequency disturbances can achieve sufficiently large amplification factors that they could potentially lead to the onset of transition over the cone. Where this onset happens will depend on the azimuthal distribution of stationary crossflow amplitudes (i.e., upon the details of the receptivity phase) and, to some extent, also upon their secondary instability characteristics. It is interesting to note that the peak N factors of the MM0 mode are less affected by azimuthal variations across the different vortices than the SI mode. This phenomenon and its implications have not been examined in detail in this paper and will be left to future studies.

The present work is an application of the PSE framework to secondary instabilities of crossflow vortices over curved, highly three-dimensional flow configurations, following the vortex trajectory within a nonorthogonal curvilinear coordinate system. The predicted amplification characteristics based on nonparallel calculations are generally consistent with those based on quasiparallel theory. The nonparallel terms associated with basic state evolution along the cone surface have a strongly destabilizing influence on the disturbance growth rates and associated N factor values. The effect of transverse curvature on the growth rates is also significant but lesser in magnitude and can be either stabilizing or destabilizing depending on the disturbance frequency. The curvature of the cone surface does appear to have a strong effect on the MM0 mode shapes when the vortex amplitude

is relatively large. In particular, the MM0 mode shapes become concentrated along the inclined shear layer corresponding to strong azimuthal gradients of the basic state. Consequently, the $|u'|$ mode shapes of MM0 modes as predicted by both the quasiparallel with-curvature theory and the plane marching PSE are rather similar to the mode shapes of the SI modes. We caution the reader, however, that all three formulations utilized in this paper involve certain approximations, particularly in converting the azimuthally inhomogeneous basic state to a locally periodic one. At present, we do not have any means of quantifying the effect of the differences between the exact and approximate basic states on the growth rates of secondary instabilities. The close match between basic state contours within the inclined shear layer suggests that the effect of this approximation should be rather small in the case of SI modes. However, because the MM0 modes are likely to be influenced by the overall vortex structure, the effect of enforcing periodicity could be slightly greater in their case.

Even for the simpler case of axisymmetric boundary layers at hypersonic speeds, whenever there are multiple unstable modes with relatively well matched phase speeds, the iterative solution to a PSE is known to have an intrinsic tendency to lock on to the most unstable mode, even if the marching process has been initialized with the subdominant mode alone. If such modal transitions were to occur in the present problem involving a considerably more complex application of the PSE, it would be difficult to determine whether they represent the true physics underlying the instability wave evolution or a numerical artifact of the PSE approximation. The latter question can again be answered only by using more sophisticated techniques and that, too, on a case-by-case basis. In principle, the QPWC and PSE approaches do include an increasing array of physical effects that were neglected during the QPNC formulation and therefore they might be expected to provide more accurate predictions. However, because of the problem complexity, the aforementioned trait of PSE marching, and the lack of prior applications of either of these approaches, we advise a more cautious approach at the present stage. Specifically, until further validation has been obtained using direct numerical simulations and/or detailed experimental measurements, we are inclined to regard the differences among the various predictions as a measure of the present uncertainty in predicting the evolution of the high-frequency secondary instabilities. Further work to assess the effects of the modeling approximations would therefore be a useful topic for future investigations, similar to a study of the effects of local phase synchronization between two different secondary instability modes.

The computations have also elucidated some of the effects of azimuthal variation across the pattern of crossflow vortices, albeit a more comprehensive analysis targeting multiple vortices and potential interactions between them is suggested for the future. Within the framework of the present set of results focused primarily on vortex 10 and, to a lesser degree, on vortex 6 and vortex 8, the MM0 modes have higher-N factors than the SI modes throughout the length of the computational domain, but the relative importance of SI modes appears to increase for crossflow vortices that are closer to the leeward plane of symmetry (namely, vortex 10 in the present case). Whether this trend is related to the manner in which the crossflow vortices were excited, i.e., to the initial amplitude spectrum, or is rather generic to the circular cone configurations at this Mach number remains to be seen. Finally, the spatial structure of the computed SI mode is similar to the measured mode shape of the intermediate-frequency modes (80–120 kHz) from the quiet tunnel experiments [25] at Texas A&M University. However, the focus of the present paper was on higher-frequency disturbances, hence the precise significance of the instability modes measured in Ref. [25] remains to be determined.

The presence of multiple SI modes in the Mach 6 configuration of interest is analogous to the secondary instability of crossflow vortices over subsonic and supersonic airfoils. Computations for the subsonic boundary layers have shown that nonlinear effects tend to reduce the growth of the secondary instability modes. However, if the amplitudes become sufficiently large, then a rapid breakdown to turbulence can ensue. Whether or not a similar scenario prevails at hypersonic Mach numbers, where the modified Mack modes also play an important role, remains to be seen. Future work should focus on the breakdown mechanisms and the strongly nonlinear phase of transition to turbulence at hypersonic speeds.

ACKNOWLEDGMENTS

This work was performed as part of the Revolutionary Computational Aerosciences discipline under the Transformational Tools and Technologies project of NASA's Transformative Aeronautics Concepts Program. Computational resources for this work were provided by the NASA High-End Computing Program through the NASA Advanced Supercomputing Division at Ames Research Center. M.C. would like to thank Professor Steven Schneider, Dr. Christopher Ward, and Joshua Edelman from Purdue University for several technical interactions. Thanks are also due to Professor William Saric and Stuart Craig from Texas A&M University for the hot wire measurements in NASA Langley Mach 6 Quiet Tunnel that helped provide a framework for the present computations. Finally, the authors acknowledge Professor Pino Martin from the University of Maryland for providing the original version of the DNS code used in this effort.

---

[1] L. M. Mack, Boundary-layer linear stability theory, AGARD Report No. 709, 1984 (unpublished).

[2] F. Li, M. M. Choudhari, C.-L. Chang, M. Wu, and P. T. Greene, *Proceedings of the 48th AIAA Aerospace Sciences Meeting Including the New Horizons Forum and Aerospace Exposition* (AIAA, Reston, 2010), paper 2010-705.

[3] W. S. Saric, H. L. Reed, and E. B. White, Stability and transition of three-dimensional boundary layers, Annu. Rev. Fluid Mech. **35**, 413 (2003).

[4] N. S. Dougherty and D. F. Fisher, *Proceedings of the 18th Aerospace Sciences Meeting* (AIAA, Reston, 1980), paper 1980-0154.

[5] R. A. King, Three-dimensional boundary-layer transition on a cone at Mach 3.5, Exp. Fluids **13**, 305 (1992).

[6] M. R. Malik and P. Balakumar, *Proceedings of the 30th Aerospace Sciences Meeting and Exhibit* (AIAA, Reston, 1992), paper 1992-5049.

[7] A. Hanifi and A. A. Dahlkild, *Proceedings of the 31st Aerospace Sciences Meeting* (AIAA, Reston, 1993), paper 1993-3048.

[8] H. Sugiura, N. Tokugawa, A. Nishizawa, Y. Ueda, H. Ishikawa, and K. Yoshida, *Proceedings of the 2003 Annual Meeting of the Japan Society of Fluid Mechanics* (JSFM, Tokyo, 2003), pp. 352–353 (in Japanese).

[9] P. Balakumar, *Proceedings of the 47th AIAA Aerospace Sciences Meeting Including the New Horizons Forum and Aerospace Exposition* (AIAA, Reston, 2009), paper 2009-3555.

[10] N. Tokugawa, M. Choudhari, H. Ishikawa, Y. Ueda, K. Fujii, T. Atobe, F. Li, C.-L. Chang, and J. White, Transition along leeward ray of axisymmetric bodies at incidence in supersonic flow, AIAA J. **53**, 3737 (2015).

[11] M. Choudhari, N. Tokugawa, F. Li, C.-L. Chang, J. White, H. Ishikawa, Y. Ueda, T. Atobe, and K. Fujii, Proceedings of the Seventh International Conference on Computational Fluid Dynamics, available at http://www.iccfd.org/iccfd7/assets/pdf/papers/ICCFD7-2306_paper.pdf

[12] C. Y. Schuele, T. C. Corke, and E. Matlis, Control of stationary crossflow modes in a Mach 3.5 boundary layer using patterned passive and active roughness, J. Fluid Mech. **718**, 5 (2013).

[13] K. F. Stetson, E. R. Thompson, J. C. Donaldson, and L. G. Siler, *Proceedings of the 23rd Aerospace Sciences Meeting* (AIAA, Reston, 1985), paper 1985-0492.

[14] S. P. Schneider, Hypersonic laminar-turbulent transition on circular cones and scramjet forebodies, Prog. Aerosp. Sci. **40**, 1 (2004).

[15] E. Swanson, Boundary-layer transition on cones at angle of attack in a Mach 6 quiet tunnel, Ph.D. thesis, School of Aeronautics and Astronautics, Purdue University, 2008.

[16] E. Swanson and S. P. Schneider, *Proceedings of the 48th AIAA Aerospace Sciences Meeting Including the New Horizons Forum and Aerospace Exposition* (Ref. [2]), paper 2010-1062.

[17] F. Li, M. Choudhari, C.-L. Chang, and J. White, *Proceedings of the 48th AIAA Aerospace Sciences Meeting Including the New Horizons Forum and Aerospace Exposition* (Ref. [2]), paper 2010-4643.

[18] P. Balakumar and L. Owens, *Proceedings of the 48th AIAA Aerospace Sciences Meeting Including the New Horizons Forum and Aerospace Exposition* (Ref. [2]), paper 2010-4718.

[19] F. Li, M. Choudhari, C.-L. Chang, J. A. White, R. Kimmel, D. Adamczac, M. Borg, S. Stanfeld, and M. Smith, *Proceedings of the 50th AIAA Aerospace Sciences Meeting Including the New Horizons Forum and Aerospace Exposition* (AIAA, Reston, 2012), paper 2012-2961.
[20] F. Munoz, D. Heitmann, and R. Radespiel, Instability modes in boundary layers of an inclined cone at Mach 6, J. Spacecraft Rockets **51**, 442 (2014).
[21] C. A. C. Ward, R. O. Henderson, and S. P. Schneider, *Proceedings of the 45th AIAA Fluid Dynamics Conference* (AIAA, Reston, 2015), paper 2015-2773.
[22] G. R. McKiernan, G. R. Chynoweth, J. B. Edelman, J. A. McKenzie, and C. J. Sweeney, *Proceedings of the 45th AIAA Fluid Dynamics Conference* (Ref. [21]), paper 2015-2317.
[23] J. Edelman and S. P. Schneider, New measurements of the secondary instability of stationary crossflow waves in the Mach-6 quiet tunnel, NATO-STO AVT-240 & RTG-082 Meeting on Hypersonic Boundary Layer Transition, Prague, Czech Republic, Oct. 15–16, 2015 (unpublished).
[24] S. A. Craig and W Saric, in *Proceedings of the Eighth IUTAM Symposium on Laminar-Turbulent Transition*, edited by M. A. F. Medeiros and J. R. Meneghini, Procedia IUTAM No. 14 (Elsevier, Amsterdam, 2015), p. 15.
[25] S. A. Craig and W. S. Saric, *Proceedings of the 45th AIAA Fluid Dynamics Conference* (Ref. [21]), paper 2015-2774.
[26] N. B. Oliviero, T. S. Kocian, A. J. Moyes, and H. L. Reed, *Proceedings of the 45th AIAA Fluid Dynamics Conference* (Ref. [21]), paper 2015-2772.
[27] S. Stanfield, R. A. Kimmel, D. Adamczac, and T. Juliano, Boundary-layer transition experiment during reentry of HIFiRE-1, J. Spacecraft Rockets **52**, 637 (2015).
[28] T. Juliano, R. A. Kimmel, S. Willems, A. Guelhan, and R Wagnild, *Proceedings of the 45th AIAA Fluid Dynamics Conference* (Ref. [21]), paper 2015-1736.
[29] F. Li, M. Choudhari, and P. Paredes, NATO-STO AVT-240 & RTG-082 Meeting on Hypersonic Boundary Layer Transition (Ref. [23]).
[30] F. Li, M. Choudhari, P. Paredes, and L. Duan, Secondary instability of stationary crossflow vortices in Mach 6 boundary layer over a circular cone, NASA Report No. NASA/TM-2015-218997, 2015 (unpublished).
[31] A. J. Moyes, P. Paredes, T. S. Kocian, and H. Reed, *Proceedings of the 54th AIAA Aerospace Sciences Meeting* (AIAA, Reston, 2016), paper 2016-0848.
[32] R. L. Kimmel, J. Poggie, and S. N. Schwoerke, Laminar-turbulent transition in a Mach 8 elliptic cone flow, AIAA J. **37**, 1080 (1999).
[33] J. Poggie and R. Kimmel, Traveling instability waves in a Mach 8 flow over an elliptic cone, AIAA J. **38**, 251 (2000).
[34] R. L. Kimmel and J. Poggie, Transition on an elliptic cone at Mach 8, American Society of Mechanical Engineers Report No. ASME FEDSM97-3111, 1997 (unpublished).
[35] M. Holden, Experimental studies of laminar, transitional, and turbulent hypersonic flows over elliptic cones at angle of attack, Air Force Office of Scientific Research Report No. AFRL-SR-BL-TR-98-0142, 1998 (unpublished).
[36] J. D. Schmisseur, S. P. Schneider, and S. H. Collicott, *Proceedings of the 37th Aerospace Sciences Meeting and Exhibit* (AIAA, Reston, 1999), paper 1999-0410.
[37] T. Juliano, E. Swanson, and S. P. Schneider, *Proceedings of the 45th AIAA Aerospace Sciences Meeting and Exhibit* (AIAA, Reston, 2007), paper 2007-0535.
[38] M. Choudhari, C.-L. Chang, F. Li, J. Edwards, and G. Candler, Hypersonic boundary layer transition: Roughness effects and 3D configurations, NASA Fundamental Aeronautics Program Annual Meeting, Atlanta, GA, October 7–9, 2008 (unpublished).
[39] K. Berger, S. Rufer, R. Kimmel, and D. Adamczak, *Proceedings of the 47th AIAA Aerospace Sciences Meeting Including the New Horizons Forum and Aerospace Exposition* (Ref. [9]), paper 2009-4055.
[40] M. Choudhari, C.-L. Chang, F. Li, K. Berger, G. Candler, and R. Kimmel, *Proceedings of the 47th AIAA Aerospace Sciences Meeting Including the New Horizons Forum and Aerospace Exposition* (Ref. [9]), paper 2009-4056.

[41] K. Berger, S. Rufer, R. Kimmel, and D. Adamczak, *Proceedings of the 47th AIAA Aerospace Sciences Meeting Including the New Horizons Forum and Aerospace Exposition* (Ref. [9]), paper 2009-4055.
[42] R. A. Kimmel, D. Adamczac, and T. Juliano, *Proceedings of the 51st AIAA Aerospace Sciences Meeting Including the New Horizons Forum and Aerospace Exposition* (AIAA, Reston, 2013), paper 2013-0377.
[43] P. Paredes and V. Theofilis, Centerline instabilities on the hypersonic international flight research experimentation HIFiRE-5 elliptic cone model, J. Fluids Struct. **53**, 36 (2015).
[44] T. Juliano, D. Adamczac, and R. A. Kimmel, HIFiRE-5 Flight Test Results, J. Spacecraft Rockets **52**, 650 (2015).
[45] T. Juliano, M. Borg, and S. P. Schneider, Quiet tunnel measurements of HIFiRE-5 boundary-layer transition, AIAA J. **53**, 832 (2015).
[46] M. Borg, R. A. Kimmel, and S. Stanfield, Traveling crossflow instability for the HIFiRE-5 elliptic cone, J. Spacecraft Rockets **52**, 664 (2015).
[47] http://vulcan-cfd.larc.nasa.gov/index.html (23 November 2009).
[48] G. D. van Albada, B. van Leer, and W. W. Roberts, A comparative study of computational methods in cosmic gas dynamics, Astron. Astrophys. **108**, 76 (1982).
[49] J. R. Edwards, A low-diffusion flux-splitting scheme for Navier-Stokes calculations, Comput. Fluids **26**, 635 (1997).
[50] D. Litton, J. Edwards, and J. White, *Proceedings of the 41st Aerospace Sciences Meeting and Exhibit* (AIAA, Reston, 2003), paper 2003-3979.
[51] F. M. Cheatwood and P. A. Gnoffo, User's manual for the Langley aerothermodynamic upwind relaxation algorithm (LAURA), NASA Report No. NASA/TM 4674, 1996 (unpublished).
[52] M. Wu and M. P. Martin, Direct numerical simulation of supersonic boundary layer over a compression ramp, AIAA J. **45**, 879 (2007).
[53] G. S. Jiang and C. W. Shu, Efficient implementation of weighted ENO schemes, J. Comput. Phys. **126**, 202 (1996).
[54] E. M. Taylor, M. Wu, and M. P. Martin, Optimization of nonlinear error sources for weighted non-oscillatory methods in direct numerical simulations of compressible turbulence, J. Comput. Phys. **223**, 384 (2006).
[55] J. Williamson, Low-storage Runge-Kutta schemes, J. Comput. Phys. **35**, 48 (1980).
[56] L. Duan, I. Beekman, and M. P. Martin, Direct numerical simulation of hypersonic turbulent boundary layers. Part 3: Effect of Mach number, J. Fluid. Mech. **672**, 245 (2011).
[57] L. Duan, M. Choudhari, and F. Li, *Proceedings of the 51st AIAA Aerospace Sciences Meeting Including the New Horizons Forum and Aerospace Exposition* (Ref. [43]), paper 2013-2617.
[58] M. Choudhari, F. Li, L. Duan, M. H. Carpenter, C. L. Streett, and M. R. Malik, *Proceedings of the 51st AIAA Aerospace Sciences Meeting Including the New Horizons Forum and Aerospace Exposition* (Ref. [43]), paper 2013-2718.
[59] F. Li and M. Choudhari, *Proceedings of the 46th AIAA Aerospace Sciences Meeting and Exhibit* (AIAA, Reston, 2008), paper 2008-590.
[60] F. Li and M. Choudhari, Spatially developing secondary instabilities in compressible swept airfoil boundary layers, Theor. Comput. Fluid Dyn. **25**, 65 (2011).
[61] P. Paredes, A. Hanifi, V. Theofilis, and D. Henningson, *Proceedings of the Eighth IUTAM Symposium on Laminar-Turbulent Transition* (Ref. [24]), p. 35.
[62] N. De Tullio, P. Paredes, N. Sandham, and V. Theofilis, Roughness-induced instability and breakdown to turbulence in a supersonic boundary-layer, J. Fluid Mech. **735**, 613 (2013).
[63] F. Li, M. M. Choudhari, M. H. Carpenter, M. R. Malik, C.-L. Chang, and C. L. Streett, *Proceedings of the 48th AIAA Aerospace Sciences Meeting Including the New Horizons Forum and Aerospace Exposition* (Ref. [2]), paper 2010-4380.
[64] F. Li, M. Choudhari, C.-L. Chang, C. L. Streett, and M. H. Carpenter, Computational modeling of roughness-based laminar flow control on a subsonic swept wing, AIAA J. **49**, 520 (2011).
[65] J. Edelman and S. P. Schneider (private communication).
[66] M. Malik, F. Li, and C.-L. Chang, Crossflow disturbances in three dimensional boundary layers: Nonlinear development, wave interaction and secondary instability, J. Fluid Mech. **268**, 1 (1994).

[67] E. B. White and W. S. Saric, Secondary instability of crossflow vortices, J. Fluid Mech. **525**, 275 (2005).
[68] P. Wassermann and M. Kloker, Mechanisms and passive control of crossflow vortex induced transition in a three-dimensional boundary layer, J. Fluid Mech. **456**, 49 (2002).
[69] G. Bonfigli and M. Kloker, Secondary instability of crossflow vortices: Validation of the stability theory by direct numerical simulation, J. Fluid Mech. **583**, 229 (2007).
[70] F. Li, M. M. Choudhari, M. H. Carpenter, M. R. Malik, C.-L. Chang, and C. L. Streett, *Proceedings of the 48th AIAA Aerospace Sciences Meeting Including the New Horizons Forum and Aerospace Exposition* (Ref. [2]), paper 2010-4380.
[71] F. Li, M. M. Choudhari, M. H. Carpenter, M. R. Malik, C.-L. Chang, and C. L. Streett, Control of crossflow transition at high Reynolds numbers using discrete roughness elements, AIAA J. **54**, 39 (2016).
[72] L. Duan, M. Choudhari, and F. Li, *Proceedings of the 51st AIAA Aerospace Sciences Meeting Including the New Horizons Forum and Aerospace Exposition* (Ref. [43]), paper 2013-2617.
[73] M. Choudhari, F. Li, L. Duan, M. H. Carpenter, C. L. Streett, and M. R. Malik, *Proceedings of the 51st AIAA Aerospace Sciences Meeting Including the New Horizons Forum and Aerospace Exposition* (Ref. [43]), paper 2013-2718.